








Universal thermodynamics of an $SU(N)$ Fermi-Hubbard model

Eduardo Ibarra-García-Padilla ^{1,*}, Sohail Dasgupta ¹, Hao-Tian Wei ¹, Shintaro Taie ², Yoshiro Takahashi ²,
Richard T. Scalettar ³ and Kaden R. A. Hazzard ¹

¹Rice Center for Quantum Materials, Department of Physics, Rice University, Houston, Texas 77005, USA

²Department of Physics, Graduate School of Science, Kyoto University, Kyoto 606-8502, Japan

³Department of Physics, University of California, Davis, California 95616, USA



(Received 9 August 2021; accepted 6 October 2021; published 21 October 2021)

The $SU(2)$ symmetric Fermi-Hubbard model (FHM) plays an essential role in strongly correlated fermionic many-body systems. In the one particle per site and strongly interacting limit $U/t \gg 1$, it is effectively described by the Heisenberg Hamiltonian. In this limit, enlarging the spin and extending the typical $SU(2)$ symmetry to $SU(N)$ has been predicted to give exotic phases of matter in the ground state, with a complicated dependence on N . This raises the question of what—if any—are the finite-temperature signatures of these phases, especially in the currently experimentally relevant regime near or above the superexchange energy. We explore this question for thermodynamic observables by numerically calculating the thermodynamics of the $SU(N)$ FHM in the two-dimensional square lattice near densities of one particle per site, using determinant quantum Monte Carlo and numerical linked cluster expansion. Interestingly, we find that for temperatures above the superexchange energy, where the correlation length is short, the energy, number of on-site pairs, and kinetic energy are universal functions of N . Although the physics in the regime studied is well beyond what can be captured by low-order high-temperature series, we show that an analytic description of the scaling is possible in terms of only one- and two-site calculations.

DOI: [10.1103/PhysRevA.104.043316](https://doi.org/10.1103/PhysRevA.104.043316)

I. INTRODUCTION

The Fermi-Hubbard model (FHM), in its original spin-1/2, $SU(2)$ symmetric form [1–4], plays a central role in the understanding of strongly correlated fermionic many-body systems. This is in part because it is one of the simplest models that captures essential features of real materials, and in part because it exhibits a variety of canonical correlated phases of matter. In the two-dimensional (2D) square lattice, it displays a metal-to-insulator crossover as well as magnetic order, and it is widely studied in the context of d -wave superconductivity [5–9].

Its generalization, the $SU(N)$ FHM, features larger spins and enhanced symmetry, and it provides insight into important strongly correlated systems. First, it is a simple limit of multi-orbital models such as those used to describe transition metal oxides [10–12], graphene's $SU(4)$ spin-valley symmetry [13], and twisted-bilayer graphene [14–19]. Second, the $SU(N)$ FHM is predicted to display a variety of interesting and exotic phases even in very special limits, such as the conventional $N = 2$ FHM, the $N = 3$ FHM [20–29], the $N = 4$ FHM at quarter filling [30,31], even values of N at half-filling [32–40], special $N \rightarrow \infty$ limits [41–45], one-dimensional (1D) chains [46–52], and the Heisenberg limit for $N = 3, 4, 5$ [11,28,53–61]. This richness is well illustrated by numerical studies of the Heisenberg limit, which describes the situation where the average number of particles per site is $\langle n \rangle = 1$ and the

interactions dominate the kinetic energy ($U \gg t$, with notation discussed below). Already in this simple limit and additionally in the simple 2D square lattice, the model is predicted to exhibit several phases of matter with novel and difficult-to-explain properties depending on the value of N . The dependence of the ground state order with N does not follow a simple pattern. This raises the question of whether and how this complicated N dependence manifests in the finite-temperature properties.

Although the $SU(N)$ FHM is a crude approximation to real materials, it has been realized to high precision by loading alkaline earth-like atoms (AEAs) into an optical lattice (OL). Fermionic AEAs (such as ^{173}Yb and ^{87}Sr) feature an almost perfect decoupling of the nuclear spin I from the electronic structure in the ground state, which gives rise to $SU(N = 2I + 1)$ symmetric interactions with deviations predicted to be of order $O(10^{-9})$ [62–66]. For that reason, by selectively populating nuclear spin projection states m_I of AEAs and loading them into an OL, experiments can engineer the $SU(N)$ FHM with N tunable, from 2, 3, ..., 10.

In recent years, experiments with ^{173}Yb in OLs have probed the $SU(N)$ FHM's interesting physics: the Mott insulator state for $SU(6)$ in three dimensions [67], the equation of state for $SU(3)$ and $SU(6)$ in three dimensions [68], nearest-neighbor antiferromagnetic (AFM) correlations in an $SU(4)$ system with a dimerized OL [69], nearest-neighbor $SU(6)$ AFM correlations in OLs with uniform tunneling matrix elements in one, two, and three dimensions [70], and recently a flavor-selective Mott insulator for $SU(3)$ [71]. Furthermore, employing quantum gas microscopy [72–78] to discriminate

*eibarragp@rice.edu

finite temperature analogs of the variety of proposed ground states [32,33,53–58] via direct observation of long-ranged correlations [70,79–81] is expected to reveal a wealth of physics. All of these experimental efforts make an understanding of the 2D square lattice thermodynamics urgent.

In contrast with most previous work that focused on the Heisenberg limit, in this work we study the $SU(N)$ FHM at finite temperature and for a range of interaction parameters, including far from the Heisenberg limit, a regime that is both interesting and experimentally important. We calculate and analyze thermodynamic properties of the model as a function of N , the interaction strength U , and the temperature T . We numerically explore the evolution of the energy, number of on-site pairs [82], and kinetic energy, as well as their derivatives in the 2D square lattice $SU(N)$ FHM at $1/N$ filling, i.e., one particle per site on average.

Some of the quantities we compute, such as the number of on-site pairs are immediately measurable in experiment, while others such as the kinetic energy and total energy are of fundamental importance and may also become accessible. For example, Ref. [83] experimentally determined the energies of a Bose-Hubbard model. In that work the kinetic energy was measured by analyzing time-of-flight images and the interaction energy was measured by site-resolved high-resolution spectroscopy. These techniques can be also used for the FHM. Additionally, in a quantum gas microscope the number of on-site pairs can be spatially resolved by generalizing the technique used in Ref. [84] to AEAAs. This would require employing an optical (rather than magnetic) Stern-Gerlach technique to split the different spin flavors into different layers, followed by detection by single-site fluorescence. Additionally, access to total density fluctuations in a bilayer quantum gas microscope, as done in Refs. [85,86], provides a route to realize thermometry without the need to comparison with numerical simulations.

We also present some selected results as a function of chemical potential μ . Results are obtained using the determinant quantum Monte Carlo (DQMC) and numerical linked cluster expansion (NLCE) methods. Here and throughout we set Boltzmann's constant to $k_B = 1$.

Although the ground state has a complicated N dependence, we find that for temperatures above the superexchange energy $T \gtrsim J = 4t^2/U$, the energy, the number of on-site pairs, and the kinetic energy depend on N in a particularly simple way, obeying a simple, analytic dependence on N .

Even though a simple scaling at very high temperatures would be unsurprising—since a low-order high-temperature series expansion (HTSE) would be expected to be accurate and to produce analytic expressions that plausibly would show simple N dependence—such expansions are insufficient to explain our findings. The HTSE is accurate only for $T \gtrsim 4t$, while the universal scaling persists to temperatures $T \gtrsim 4t^2/U$ that are much lower when $U \gg t$. At such temperatures the HTSE not only is inaccurate but diverges.

Despite the failure of the HTSE to fully explain the observations, a simple explanation is possible by recognizing that correlations are short-ranged in this temperature regime. We show that in this limit, the second-order NLCE accurately reproduces the results and the N scaling relation. Furthermore, under controlled approximations in the $J \ll T \ll U$ regime

one can analytically evaluate the pertinent contributions based on the NLCE, and with this explain the observed universal scaling with N to zeroth order in βJ . This demonstrates the utility of the NLCE framework for analytic calculations, beyond its typical application in numerical calculations. These observations show that the one- and two-site correlations control the physics deep in this regime.

The remainder of this paper is organized as follows: Sec. II presents the $SU(N)$ Hubbard Hamiltonian, defines the observables we consider, and presents details of the numerical and analytical methods used. Section III presents the main results, and Sec. IV concludes.

II. MODEL AND METHODS

A. The $SU(N)$ Hubbard Hamiltonian and observables

The $SU(N)$ FHM is defined by the grand canonical Hamiltonian

$$H = -t \sum_{\langle i,j \rangle, \sigma} (c_{i\sigma}^\dagger c_{j\sigma} + \text{H.c.}) + \frac{U}{2} \sum_{i, \sigma \neq \tau} n_{i\sigma} n_{i\tau} - \mu \sum_{i, \sigma} n_{i\sigma}, \quad (1)$$

where $c_{i\sigma}^\dagger$ ($c_{i\sigma}$) is the creation (annihilation) operator for a fermion with spin flavor $\sigma = 1, 2, \dots, N$ on site $i = 1, 2, \dots, N_s$ in a 2D square lattice, N_s denotes the number of lattice sites, $n_{i\sigma} = c_{i\sigma}^\dagger c_{i\sigma}$ is the number operator for flavor σ , t is the nearest-neighbor hopping amplitude, U is the interaction strength, and μ is the chemical potential that controls the fermion density.

We are interested in thermodynamic quantities such as the number of on-site pairs per site

$$\mathcal{D} = \frac{1}{N_s} \sum_i \left[\frac{1}{2} \sum_{\sigma \neq \tau} \langle n_{i\sigma} n_{i\tau} \rangle \right], \quad (2)$$

the kinetic energy per site

$$K = \frac{1}{N_s} \left\langle -t \sum_{\langle i,j \rangle, \sigma} (c_{i\sigma}^\dagger c_{j\sigma} + c_{j\sigma}^\dagger c_{i\sigma}) \right\rangle, \quad (3)$$

the energy per site $E = \langle H/N_s + \mu n \rangle$ (where $n = (1/N_s) \sum_{i, \sigma} n_{i\sigma}$), and the entropy S . We present these observables and the derivatives dE/dT , dK/dT , and $Ud\mathcal{D}/dT$ as functions of T/t for different values of the interaction strength U/t either as a function of chemical potential μ/t or at fixed density $\langle n \rangle = (1/N_s) \sum_{i, \sigma} \langle n_{i\sigma} \rangle = 1$. We also show the compressibility $\kappa = d\langle n \rangle/d\mu$ as a function of μ for various T/t , U/t , and N . These observables provide valuable knowledge about the physics: the number of on-site pairs is a useful measure of the Mott insulating nature of the system, the kinetic energy of its spatial coherence, and the entropy and specific heat provide information about the temperature scales at which various degrees of freedom cease to fluctuate.

B. Numerical methods

To calculate the thermodynamic observables, we employ two numerical techniques, DQMC [87,88] and NLCE [89,90], which have complementary strengths, and compare in some cases with low-order analytic HTSE and the noninteracting

limit. The DQMC and NLCE are often the numerical methods of choice for the SU(2) FHM in the finite-temperature regime studied in ultracold matter [91–95], and we use our extensions of these methods to SU(N) systems [70]. Generally speaking, the DQMC will perform best at weak to intermediate interactions, while the NLCE performs best at strong interactions; we present both methods where both are viable.

1. Determinant quantum Monte Carlo (DQMC)

Averages of the thermal equilibrium observables are evaluated with DQMC on 6×6 lattices by introducing $N(N-1)/2$ auxiliary Hubbard-Stratonovich fields, one for each interaction term [96]. In this method, the inverse temperature β is discretized in steps of $\Delta\tau$ with a Trotter step $\Delta\tau = 0.05/t$ for $U/t = 4, 8$ and $\Delta\tau = 0.04/t$ for $U/t = 12$. In order to obtain accurate results, we obtain DQMC data for 40–60 different random seeds for $T/t \leq 4$ and for 2–10 different random seeds for $T/t > 4$. For each Monte Carlo trajectory we perform 2000 warm-up sweeps and 8000 sweeps for measurements [97]. In addition, the number of global moves per sweep to mitigate possible ergodicity issues [98] is set to two for $U/t = 4, 8$ and to four for $U/t = 12$. These global moves update, at a given lattice site, all the imaginary time slices that couple two spin flavors. DQMC results presented in the paper are obtained by computing the weighted average and weighted standard error of the mean of the results obtained by using different random seeds. We use the inverse squared error of each measurement as their weight. Results obtained using a uniform weight for all measurements yield consistent results but with larger error bars (~ 2 -4 times larger). Estimates of systematic errors are obtained for $N = 6$ at $U/t = 12$ (Trotter) and $N = 6$ at $U/t = 4$ (finite-size), where they are expected to be worst. We estimate the Trotter error by comparing the results obtained with $\Delta\tau = 0.04/t$ and $\Delta\tau = 0.05/t$. Their difference is below 4% for all observables of interest at $T/t = 0.5$. This discretization error is even smaller at higher temperatures and for the other two values of U/t considered. Finite-size errors are estimated by comparing results for different thermodynamic quantities in 4×4 and 6×6 lattices. At $T/t = 0.5$ their differences are $\lesssim 6.5\%$ for $U/t = 4$ and $\lesssim 5.7\%$ for $U/t = 12$.

2. Calculation of specific heat and entropy in DQMC

For DQMC data we evaluate the specific heat and entropy in two ways. In the first approach, we numerically differentiate the energy to obtain the specific heat (see [99] for details on the differentiation procedure), and we compute the entropy by integrating $dS = dQ/T = C/T dT$, with $C = dE/dT$ the specific heat. Integrating by parts, S can be rewritten in terms of the energy E ,

$$S(T) = S_\infty + \frac{E(T)}{T} - \int_T^\infty \frac{E(T')}{T'^2} dT', \quad (4)$$

where S_∞ is the entropy at fixed density in the limit when $T \rightarrow \infty$ (see Appendix A for more details).

The DQMC starts becoming unreliable at T below the superexchange scale J . In this regime the statistical noise increases due to the sign problem, severely limiting calculations. In addition to presenting the DQMC calculations directly, we

also show results obtained from fitting and from differentiating this smooth fit function, which can reduce the noise at the cost of potentially biasing the data. For the energy, we fit to the simple functional form [100,101],

$$E(T) = E(0) + \sum_{k=1}^M c_k e^{-\beta k \Delta}, \quad (5)$$

with fitting parameters c_k , Δ , and $E(0)$. The number of parameters c_k , M , is chosen to be around 6–12 (slightly less than one-third of the data points to be fit), which is similar to Refs. [100,101]. We smooth the 10 lowest temperature data points using a moving average with a three-point window fitted with a local first-order polynomial (Savitzky-Golay filter). Then the data are fit with Eq. (5), by choosing the fitting parameters that minimize

$$\Xi^2 = \frac{1}{N_p + 1} \left(\sum_{n=1}^{N_p} [E(T_n) - E_n]^2 + \left[S_\infty - \sum_{k=1}^M \frac{c_k}{k\Delta} \right]^2 \right), \quad (6)$$

where N_p is the number of data points, and E_n is the DQMC energy at T_n . The first term ensures a good fit of the data, while the second term regularizes the fit and ensures that $S \rightarrow 0$ as $T \rightarrow 0$ by enforcing the constraint $S_\infty = \int_0^\infty \frac{C(T')}{T'} dT' = \sum_{k=1}^M \frac{c_k}{k\Delta}$ [102]. A similar procedure is used to obtain fits for the number of on-site pairs and the kinetic energy: Each data set is fit using the same form as Eq. (5), subject to the constraint that the derivative of their sum obeys the specific heat sum rule.

Results obtained from fitting remove the noise providing smooth guides to the eye. By construction they also satisfy important physical features such as sum rules. However, fitting necessarily biases the results and should be interpreted with caution. Care is especially warranted in the high-noise regimes (mainly occurring in the derivative data at the lowest temperatures presented) where the fits are used to extrapolate the data. Nevertheless, the fits suggest interesting features and trends that may help guide future low-temperature calculations and experiments.

3. Numerical linked cluster expansion (NLCE)

Thermodynamic observables are computed using a fifth-order site expansion NLCE. We briefly derive and present this algorithm, which is reviewed in Ref. [90]. Extensive properties in a lattice are evaluated by performing a weighted sum of their value in all possible clusters c embeddable in the lattice; specifically,

$$P(\mathcal{L})/N_s = \sum_{c \in \mathcal{L}} L(c) W_P(c), \quad (7)$$

where $P(\mathcal{L})$ is the property evaluated on the entire lattice \mathcal{L} , N_s is the number of lattice sites, $L(c)$ is the number of ways that the cluster c can be embedded in the lattice (up to translation invariance), and $W_P(c)$ is defined as

$$W_P(c) = P(c) - \sum_{s \subset c} W_P(s). \quad (8)$$

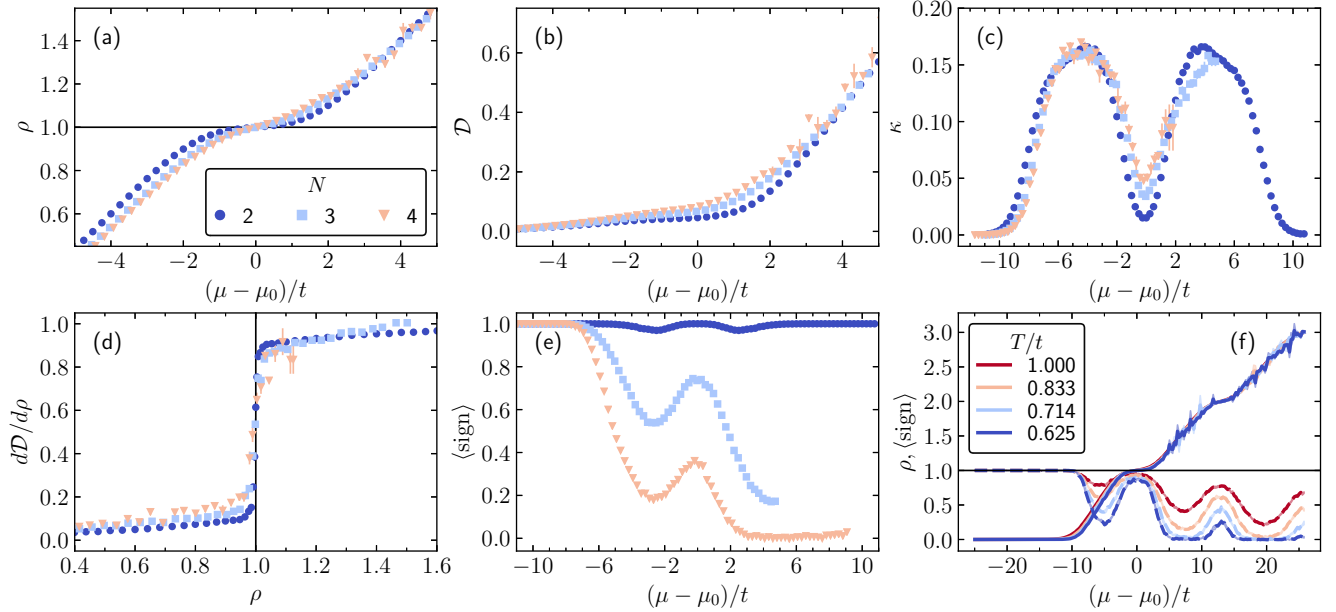


FIG. 1. Density's, number of on-site pairs', compressibility's, and determinantal sign's dependence on chemical potential. Panels (a)–(e) compare observables for $N = 2, 3, 4$ for $U/t = 8$ at $T/t = 0.5$ as functions of the chemical potential $(\mu - \mu_0)/t$, where $\rho(\mu_0) = 1$. (a) Density; there is a clear softening of the Mott plateau as N increases. (b) Number of on-site pairs. (c) Compressibility. (d) Derivative of the number of on-site pairs with respect to the density as a function of density. (e) Average sign. (f) Density (solid) and average sign (dashed) vs $(\mu - \mu_0)/t$ for different values of T/t for $N = 6$ at $U/t = 12$. Shaded regions correspond to error bars.

Equation (7) follows directly from the definition of the $W_P(c)$. Equation (7) is an infinite sum over all clusters, and the key idea of the NLCE is to truncate this sum to clusters of small size (different variants use different measures of size) and evaluate properties on each cluster using exact diagonalization (ED). Here we truncate the sum over clusters based on the number of sites, performing calculations up to five site clusters, which shows good convergence (see Appendix B).

The Hilbert space dimension increases rapidly with N , limiting the size of clusters that can be included in the expansion, and we use multiple methods to reduce the computational cost in order to reach five-site clusters for $SU(6)$. The most straightforward is to account for the $SU(N)$ symmetry, in particular its abelian symmetries (the N conserved flavor numbers) and the flavor permutation symmetry. Additionally, for $N = 6$, we truncate the Hilbert space in the Fock basis using two criteria: (1) we include only basis states with a number of particles below a cutoff value (chosen to be six, which is one larger than the number of sites in the largest cluster) and (2) we include only basis states whose interactions energy is less than a cutoff value (chosen to be $3U$). These choices provide highly accurate (several decimal places) results over the temperature and density ranges of interest in this paper, though at high temperatures or densities they can break down. Appendix C provides details of these truncations and the calculations' convergence [103].

The NLCE is much more accurate than an exact diagonalization (ED) that uses the same number of (or even more) sites. At all temperatures considered, the five-site NLCE calculations are dramatically more accurate than 3×2 ED calculations in either periodic or open boundary conditions to quite low temperatures. In fact, at least for temperatures

where the NLCE is convergent and the density $\langle n \rangle = 1$ case that is our main focus, even a two-site NLCE calculation outperforms the 3×2 ED, despite requiring enormously fewer computational resources. We note that this is, to our knowledge, the first application of NLCE to the $SU(N)$ FHM. The convergence with expansion order and comparisons with ED are discussed in Appendix B.

The NLCE self-diagnoses its accuracy, with converged results expected when adjacent orders give nearly the same answer. Results in the main text are presented for the highest order computed and the NLCE data is cutoff at temperatures where the three highest consecutive orders deviate more than 2%.

4. Low-order high-temperature series expansions (HTSEs)

It is useful to compare computed observables against simple analytic zeroth- and second-order high-temperature series in t/T [104]. The region of validity of the HTSE to any order is $T \gtrsim t$, yielding unphysical results for $T \lesssim t$.

III. RESULTS

This section presents our main results, the calculation of several thermodynamic observables, and analysis of features observed in them, especially their striking universal N dependence. Specifically, we calculate the number of on-site pairs \mathcal{D} , the kinetic energy K , the energy E , the entropy S , the specific heat C , and the contributions to it from the interaction and kinetic energies $Ud\mathcal{D}/dT$, and dK/dT , respectively, all defined previously. Mostly we focus results at a density $\langle n \rangle = 1$, but some results are also presented as a function of chemical potential μ/t , which causes the density to vary.

This section is organized as follows: Sec. III A presents the μ/t dependence of $\langle n \rangle$, \mathcal{D} , the compressibility $\kappa = \partial \langle n \rangle / \partial \mu$, and the determinantal sign. The following subsections present the U/t , T/t , and N dependence of \mathcal{D} (Sec. III B), K (Sec. III C), and E (Sec. III D). Section III E presents the scaling collapse demonstrating the universal N dependence of E , \mathcal{D} , and K . Section III F presents the temperature derivatives. Finally Sec. III G presents the U/t , T/t , and N dependence of S . Results in Secs. III B to III G are all at unit density.

A. Density, number of on-site pairs, compressibility, and determinantal sign dependence on chemical potential μ/t

Figures 1(a) and 1(b) show the dependence of density $\rho = \langle n \rangle$ and number of on-site pairs \mathcal{D} on the chemical potential. These are particularly important quantities because typical experiments on ultracold atoms use smooth traps, and the μ dependence of the observables is related to their spatial dependence by the local density approximation [105]. These are also among the most straightforward observables to measure and have been explored experimentally as a function of U/t , N , μ/t , and T/t in Refs. [67,68].

The density as a function of chemical potential shows a Mott plateau—a region of μ over which the density is nearly constant—when the temperature is $T \lesssim U$, as shown in Fig. 1(a), signaling the incompressible and insulating nature of the system. At fixed temperature, the Mott region becomes less sharply defined as N increases. This is expected, as increasing N allows for more density fluctuations at a given energy and thus a more compressible system at a fixed temperature [as corroborated by Fig. 1(c)]. This behavior is also observed for $U/t = 12$ at the same temperature (not shown here as to not overcrowd Fig. 1). The general trend is already seen in the second-order HTSE [104] and was observed experimentally in Ref. [68].

Although the Mott plateau softens with increasing N , appearing only as a subtle shoulder for $N = 4$ at $U/t = 8$ and $T/t = 0.5$, if one plots $d\mathcal{D}/d\rho$ as a function of ρ , there is a quite sharp and clear signature of the Mott plateau for all cases, as shown in Fig. 1(d).

We also show the average determinantal sign, which characterizes the sign problem, one of the fundamental limitations to quantum Monte Carlo calculations of interacting fermions [106–108]. For the type of Hubbard-Stratonovich decomposition used in the current study for DQMC, we find the average sign decreases (i.e., the sign problem worsens) overall as N increases and as the temperature is lowered [see Figs. 1(e) and 1(f)]. On top of this, the sign problem is worse for the metallic phase than the Mott insulating phase at a fixed temperature. Figure 2(a) shows that at fixed T/t , increasing U/t worsens the sign problem in the metal, but improves it in the insulator in the currently studied temperature regime. The $N = 2$ case is free of the sign problem at half-filling, and therefore $\langle \text{sign} \rangle = 1$ when $\langle n \rangle = 1$ for all values of U/t .

Finally, the U/t dependence of κ for different N is displayed in Fig. 2(b). As the U/t increases, the system becomes more incompressible where $\langle n \rangle = 1$, highlighting the insulating nature of the system. Our results are in agreement with qualitative trends identified in previous dynamical mean-field theory (DMFT) results [109].

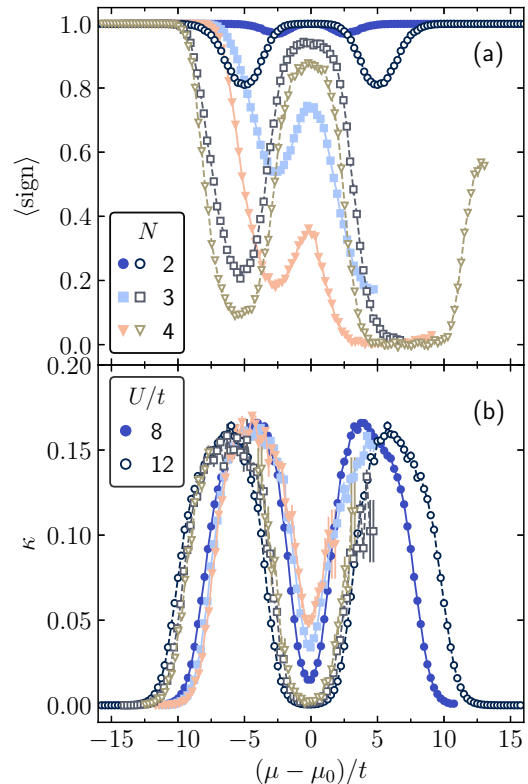


FIG. 2. Determinantal signs' and compressibility's dependence on interaction strength. (a) Average sign and (b) compressibility vs $(\mu - \mu_0)/t$, where $\rho(\mu_0) = 1$ for $U/t = 8$ (solid markers) and $U/t = 12$ (open markers) for $N = 2, 3, 4$ at $T/t = 0.5$.

B. Number of on-site pairs at unit density: Dependence on U/t , T/t , and N

The number of on-site pairs \mathcal{D} decreases as temperature is lowered, almost always followed by an increase at the lowest temperatures. These features show clear trends with U/t and N as shown in Fig. 3. The trends with U/t are that, as the temperature is lowered, (1) \mathcal{D} is suppressed from its high-temperature value at a temperature scale $T \sim U$, and (2) \mathcal{D} increases at a much lower temperature that decreases with increasing U/t . Also, as expected, overall larger U/t leads to smaller \mathcal{D} , most strongly in the temperature window between the two features discussed previously. The trends with N are also clear: (1) as N increases, \mathcal{D} increases, (2) the temperature at which the low- T increase of \mathcal{D} occurs is roughly independent from N except for $U/t = 8$, where is higher for larger N , and (3) the increase of \mathcal{D} as the temperature is decreased through the lower temperature feature is larger for larger N . For sufficiently large U/t , the dependence on N is weaker, as shown in Fig. 3(a). These features will be explained below.

Although the temperatures are not extremely low, $T \gtrsim 0.1t$, the qualitative features are not captured with a low-order HTSE, as shown in Fig. 3(a), which diverges from the true results at $T/t \sim 3$ or larger. Furthermore, for the temperature regions where NLCE and DQMC are well converged, both methods are in good agreement, supporting the validity and convergence of the different approaches.

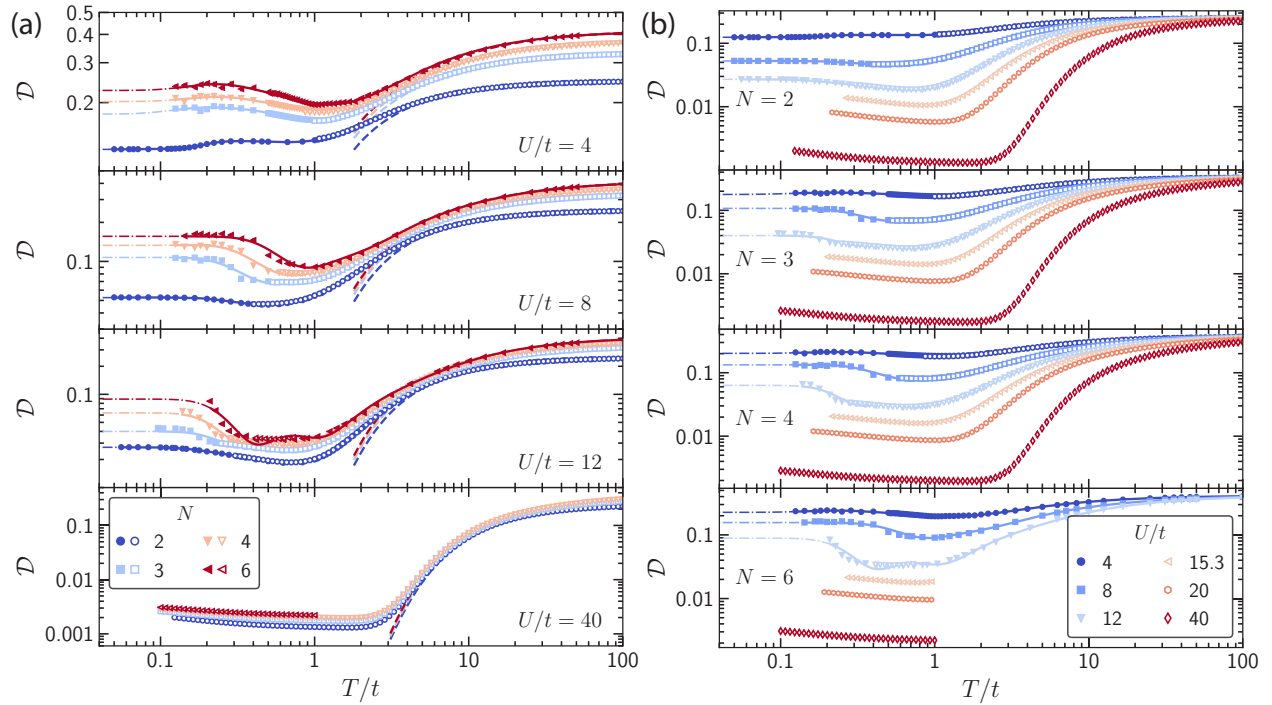


FIG. 3. Number of on-site pairs \mathcal{D} versus temperature. (a) Each panel compares \mathcal{D} for $N = 2, 3, 4, 6$ for a fixed U/t at $(n) = 1$. (b) Each panel compares \mathcal{D} for $U/t = 4, 8, 12, 15.3, 20, 40$ for a fixed N . Solid markers are DQMC, open markers are NLCE, dashed lines are the zeroth-order HTSE, and solid lines are the fits of Eq. (5) to the DQMC data down to the lowest T_n point. Thinner dash-dotted lines come from the fit in the extrapolated regime $T < \min(T_n)$, where $\{T_n\}$ is the data set of temperatures where DQMC results are obtained.

The T , N , and U dependence of \mathcal{D} can be qualitatively understood by considering the two-site, two-particle (TSTP) system, which was employed to understand similar features in the $N = 2$ anisotropic lattice calculations of Ref. [110]. We begin by describing the T dependence. For $T \gtrsim U$, eigenstates with energy $\sim U$ and a large fraction of double occupancies are occupied. As the temperature is lowered below U , the eigenstates dominated by one-particle-per-site configurations have the largest Boltzmann weight and have small admixture of doublons, thus explaining the high-temperature decrease of \mathcal{D} upon cooling. The more interesting low-temperature increase of \mathcal{D} is explained by considering the physics in this sector dominated by one-particle-per-site configurations. In this sector, these low-energy eigenstates are approximately “SU(2) singlets” on the two sites [$\propto(|\sigma, \tau\rangle - |\tau, \sigma\rangle)$ with $\sigma \neq \tau$] or “SU(2) triplets” [$\propto(|\sigma, \tau\rangle + |\tau, \sigma\rangle)$ where τ and σ may be equal]. The “singlet” states include an admixture $\propto (t/U)^2$ of doublons, which allows for some delocalization, lowering the kinetic energy and therefore lowering the energy of singlet states relative to the triplet ones, which have no admixture of doublons. Therefore, as the temperature is lowered below the energy scale splitting the singlet and triplet configurations, the system populates the singlet states and the number of double occupancies increases until it saturates. This low-temperature population of SU(2) singlets also leads to the antiferromagnetic correlations observed in Ref. [70].

The dependence of \mathcal{D} on N can also be understood in this picture, by considering the number of available ways to form an on-site pair. Since the number of possible configurations of m particles on a single site is $\binom{N}{m}$, the number of on-site pairs

is enhanced for $N > 2$ for all values of the interaction strength and temperature due to thermal fluctuations and quantum fluctuations (tunneling) [111].

This argument provides an understanding of the overall trends of \mathcal{D} with T and N , but the $U = 4t$, $N = 2$ curve is worth further consideration as the sole curve that does not show the low-temperature increase. The reason for this is not obvious: that a low-temperature rise would be smaller for small N is explained above, but that it actually turns from a rise to a decrease is not. We note that this is likely a special feature of not only $N = 2$ and small U/t , but also 2D systems, as when the system is perturbed away from 2D a low-temperature rise in \mathcal{D} appears [110]. As such, it is natural to conjecture it is related to Fermi surface nesting (see Fig. 4), which is most important at small U/t , and which is perfect only for $N = 2$.

C. Kinetic energy at unit density: Dependence on U/t , T/t , and N

The kinetic energy K shows features at similar energy scales as \mathcal{D} , as shown in Fig. 5. At high temperatures, the kinetic energy vanishes, and decreases as the temperature is lowered, in close agreement with the noninteracting calculations (described momentarily) until $T \sim U$. At $T \lesssim U$ the kinetic energy becomes smaller in magnitude than the noninteracting limit by an amount that increases with U . Finally, at the lower temperature scale on which \mathcal{D} rises again, the kinetic energy drops significantly, signaling the same tunneling processes that create doublons, explained at the end of Sec. III B.

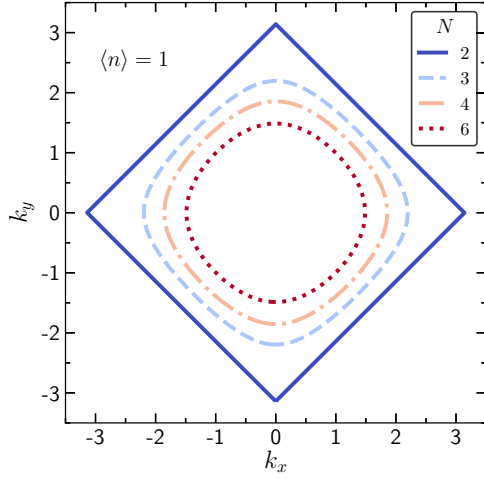


FIG. 4. Fermi surface for $N = 2, 3, 4, 6$ in the $U = 0$ 2D square lattice at $\langle n \rangle = 1$.

The noninteracting limit's behavior is straightforward to understand: for $N = 2$ and $\langle n \rangle = 1$, the Fermi surface is a perfect square (Fig. 4), and as N is increased this shrinks and becomes circular. Thus the kinetic energy decreases as N increases. Figure 5 shows the noninteracting limit results

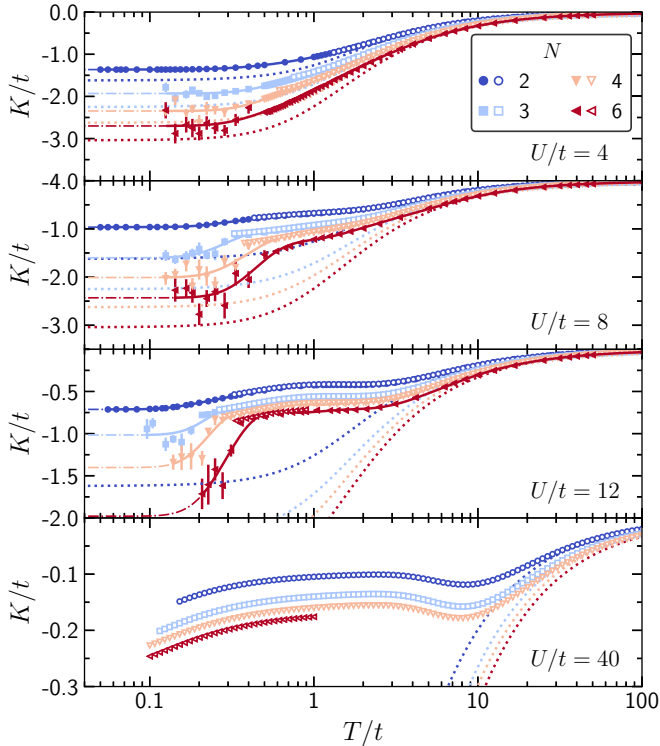


FIG. 5. Kinetic energy vs temperature. Each panel compares K for $N = 2, 3, 4, 6$ for a fixed U/t at $\langle n \rangle = 1$. Solid markers are DQMC, open markers are NLCE, dotted lines correspond to the noninteracting limit, and solid lines are the fits of Eq. (5) to the DQMC data down to the lowest T_n point. Thinner dash-dotted lines come from the fit in the extrapolated regime $T < \min(T_n)$, where $\{T_n\}$ is the data set of temperatures where DQMC results are obtained.

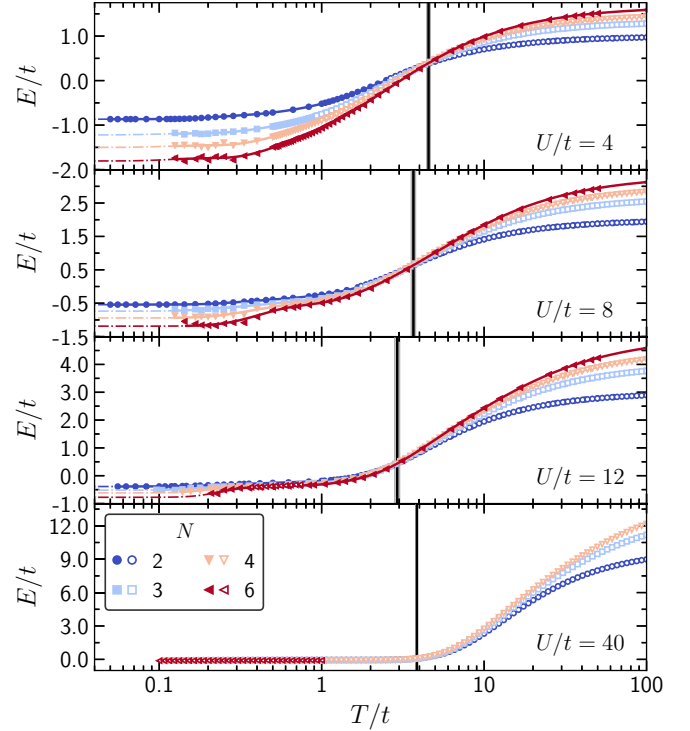


FIG. 6. Energy vs temperature. Each panel compares E for $N = 2, 3, 4, 6$ for a fixed U/t at $\langle n \rangle = 1$. Solid markers are DQMC, open markers are NLCE, solid lines are the fits of Eq. (5) to the DQMC data down to the lowest T_n point. Thinner dash-dotted lines come from the fit in the extrapolated regime $T < \min(T_n)$, where $\{T_n\}$ is the data set of temperatures where DQMC results are obtained. Vertical regions in black indicate the temperature window where the different N curves intersect.

(dotted line)

$$K = \frac{1}{(2\pi)^2} \int_{\text{BZ}} \frac{\epsilon_{\vec{k}} d^2k}{e^{\beta(\epsilon_{\vec{k}} - \mu)} + 1}, \quad (9)$$

where the integral is over the Brillouin zone and $\epsilon_{\vec{k}} = -2t(\cos k_x + \cos k_y)$ is the noninteracting dispersion (setting the lattice constant to unity). The chemical potential μ is determined numerically to give $\langle n \rangle = 1/(2\pi)^2 \int_{\text{BZ}} d^2k / (e^{\beta(\epsilon_{\vec{k}} - \mu)} + 1) = 1$.

D. Total energy at unit density: Dependence on U/t , T/t , and N

The total energy $E = UD + K$ (Fig. 6) shows features simply related to D and K . However, a new and surprising feature appears in E : the curves for different N cross at a temperature and energy (T^*, E^*) with $t < T^* < U$. Figure 7 shows that T^* first decreases then increases as a function of U/t , while E^* first increases, then decreases. In Sec. III E we will see that this crossing is a consequence of an even more dramatic phenomena—a universal collapse upon rescaling over a broad temperature range.

The existence and qualitative trends of the crossing can be understood again by the system with two sites and two particles (TSTP) and can be quite accurately described by the second-order NLCE, whose only inputs are the one- and

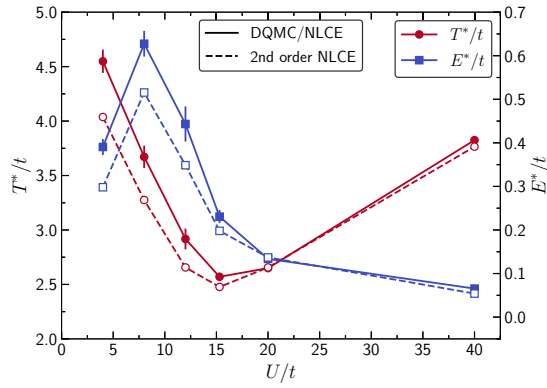


FIG. 7. Interaction dependence of the energy crossing. Temperature (red circles) and energy (blue squares) where the curves for different N cross in Fig. 6. Error bars correspond to the width of the crossings. Dashed lines correspond to the second-order NLCE.

two-site exact diagonalization calculations (a point we will revisit in Sec. III E).

Within the TSTP, the crossing occurs when $E^* = 0$, indicating that for all N 's, their kinetic and interaction energies cancel each other at the same T^* (see Appendix D for details). When we include higher particle numbers in the two-site problem, there is a small contribution to the energy from eigenstates that present multiple double occupancies and/or higher-than-double occupancies. Their contribution accounts for a constant positive shift in the energy for all N 's, implying that the crossing occurs at $E^* > 0$. The second-order NLCE is a linear combination of the one- and two-site results. The one-site result contributes another constant positive shift for all N 's to E . Together, the second-order NLCE clearly reproduces the trends displayed in Fig. 7, where we present E^* and T^* as a function of the interaction strength.

E. Universal N dependence of energy, number of on-site pairs, and kinetic energy

In this section, we show that the crossing point of E vs T for all N in Fig. 6 is actually a consequence of a much stronger universal scaling relation that determines the N dependence of all the observables studied here to temperatures well below the crossing temperature (though not arbitrarily low), down to a temperature comparable to the superexchange energy $4t^2/U$. We find that the energy satisfies

$$E(T, N) = E(T, \infty) + (1/N)E_1(T) \quad (10)$$

for some $E_1(T)$ independent of N over a broad range of temperature. This is shown in Fig. 8 by a universal collapse of appropriately constructed quantity \tilde{E} , and we will discuss the features of this collapse more momentarily. First, to understand \tilde{E} 's construction, note that Eq. (10) is equivalent to

$$\tilde{E}(T, N) \equiv E(T, N) - (1/N)E_1(T) \quad (11)$$

being independent of N , since the right-hand side is simply $E(T, \infty)$. Figure 8 plots this \tilde{E} , taking

$$E_1(T) = \frac{E(T, N_1) - E(T, N_2)}{(1/N_1) - (1/N_2)} \quad (12)$$

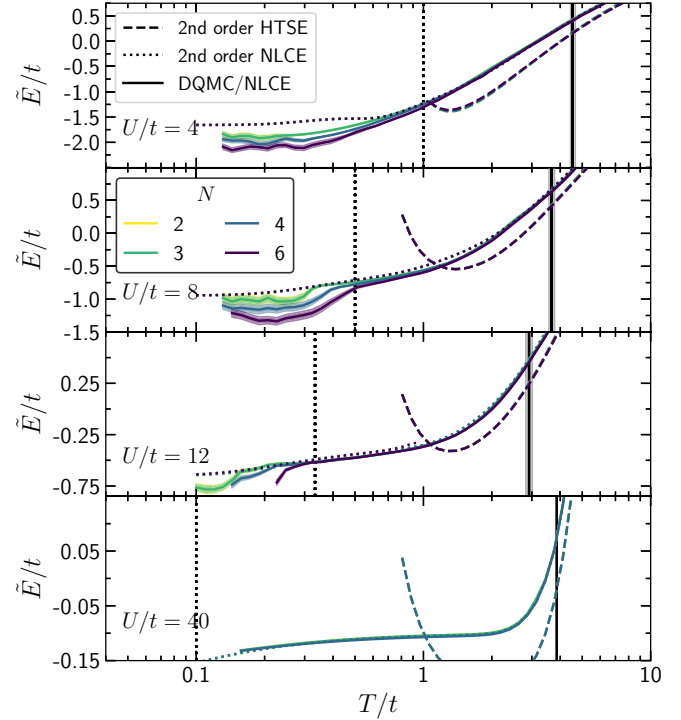


FIG. 8. Universal dependence of energy on N . \tilde{E} vs temperature for several N at fixed $U/t = 4, 8, 12$ at $\langle n \rangle = 1$. Solid lines correspond to numerical data: DQMC for $U/t = 4, 8, 12$ and NLCE for $U/t = 40$. Shaded regions correspond to error bars obtained by error propagation in Eq. (11). Dashed lines correspond to second-order HTSE calculations, and dotted lines correspond to second-order NLCE. Solid vertical lines indicate the temperature where the different N curves intersect, and dotted vertical lines indicate the superexchange energy J .

for $N_1 = 2$ and $N_2 = 3$. When Eq. (10) is satisfied, the $E_1(T)$ obtained would be the same for all choices of N_1 and N_2 ; we choose $N_1 = 2$ and $N_2 = 3$ as they are the least noisy data sets and span the largest range of temperatures, but the overall collapse is observed independent of this choice. The analysis of scaling is inspired by similar scalings discovered in the spectra of strongly correlated materials in Ref. [112]. We observe that Eq. (10) has the form of a first-order Taylor expansion of $E(T, N)$ in $1/N$; from this point of view, the remarkable aspect of the data collapse is that (in an appropriate temperature window) it accurately describes the physics even when $1/N$ is not small (e.g., for $N = 2$).

Figure 8 shows that \tilde{E} is independent of N at temperatures $T \gtrsim J \equiv 4t^2/U$ for all U studied here, and therefore $E(T, N)$ has the simple N dependence given by Eq. (10). Below $T \sim J$, \tilde{E} no longer collapses, signaling a more complicated N dependence. One consequence of the universal scaling is that the thermodynamics in this temperature regime can be obtained for any N from the results for $N = 2$ and 3 (or any two N). This is convenient for several reasons: the Hilbert space of $SU(2)$ is more manageable for numerical calculations, and because numerical methods such as DQMC are free of the sign problem at $\langle n \rangle = 1$ for $SU(2)$.

One natural attempt to explain the observed scaling would be the HTSE, since this is expected to be accurate at

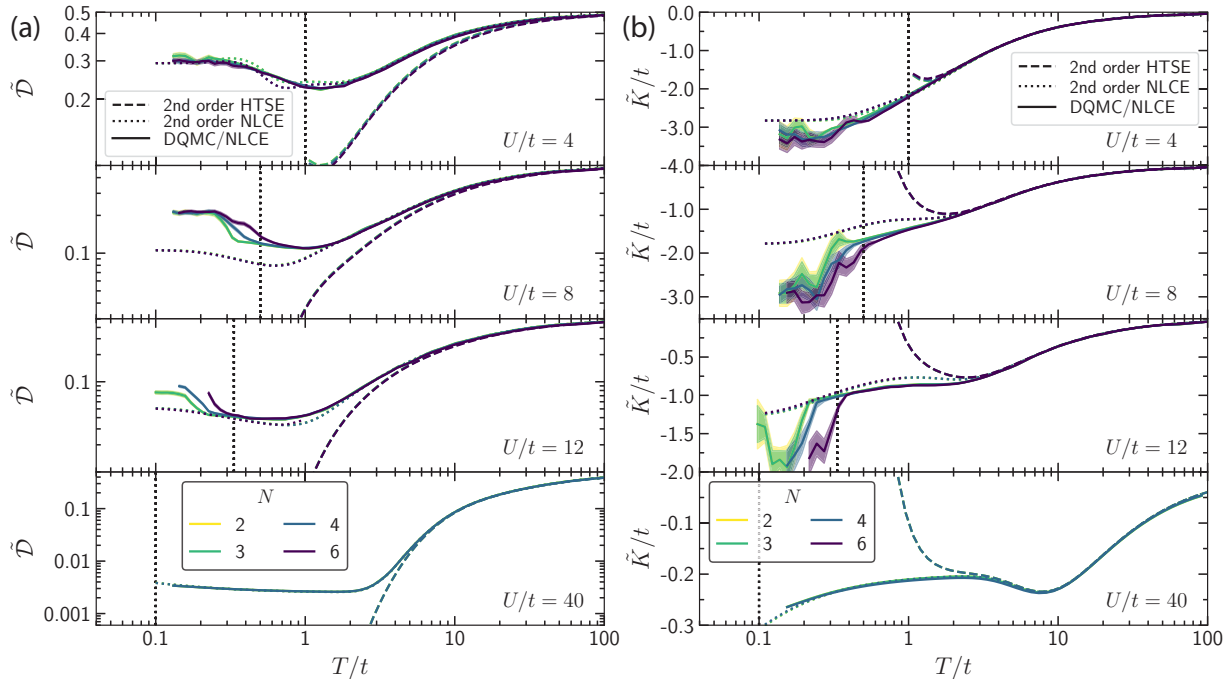


FIG. 9. Universal dependence of number of on-site pairs and kinetic energy on N . (a) \tilde{D} and (b) \tilde{K} vs temperature for several N at fixed $U/t = 4, 8, 12$ at $\langle n \rangle = 1$. Solid lines correspond to numerical data: DQMC for $U/t = 4, 8, 12$ and NLCE for $U/t = 40$. Shaded regions correspond to error bars obtained by error propagation in analogs of Eq. (11). Dashed lines correspond to second-order HTSE calculations, and dotted lines correspond to second-order NLCE. Dotted vertical lines indicate the superexchange energy J .

high temperatures; however, although \tilde{E} calculated with the second-order HTSE collapses, it deviates strongly from the data at $T \lesssim 5t$ (Fig. 8), so it cannot explain the collapse to the lowest temperatures observed ($0.1t$ to t , depending on the value of U). In contrast, as Fig. 8 shows, the second-order NLCE's \tilde{E} not only collapses, but accurately reproduces the numerical results for all temperatures where the collapse occurs, thus providing a simple and effectively complete calculational tool to obtain the scaling, albeit not an analytic one. That the second-order NLCE reproduces the data in the scaling regime allows us to infer characteristics of the physics. The first thing to notice is that the second-order NLCE can capture one- and two-site nearest-neighbor correlations, but no longer-ranged correlations. Thus, one-site physics and nearest-neighbor correlations suffice to capture the physics in the regime where collapse occurs. This provides interesting insight into the physics and explains why the collapse occurs at $T \gtrsim J$: this is the characteristic energy scale for correlations in the $\langle n \rangle = 1$ system (at least when U/t is large) and thus longer range correlations develop only at temperatures below J . Note that this also lets us understand why the collapse is not captured by the second-order HTSE: this misses two-site correlations that are $O(\beta t)^3$ or higher. Such nonperturbative effects are strong in the regime $4t^2/U \lesssim T \lesssim t$ and not easily captured at any order of the HTSE, which diverges for $T \lesssim t$.

By examining the second-order NLCE and simplifying it by taking advantage of the range of temperatures being considered, we can also arrive at an analytic explanation of the scaling phenomena. Although NLCE is typically used as a numerical method, at low-enough order and in simplified limits, it may provide simple analytic expressions. Indeed, in

the present case, we show in Appendix D that the energy in the second-order NLCE in the temperature range $4t^2/U \ll T \ll U$ is given, to zeroth order in βJ , by

$$E(T, U, N) \approx -J + \frac{1}{N}J. \quad (13)$$

We note the additional condition that $T \ll U$ not previously noted; indeed, there are small deviations of the data from collapsing in the $T \sim U$ regime. Finally, when $T \gg U$ the collapse is again recovered, since $K \rightarrow 0$ and $D \propto 1/N$ in that regime (see [111]). In summary, the parametrically accurate collapse for the two separate regimes $4t^2/U \ll T \ll U$ and $T \gg U$ is interpolated to a quite accurate collapse, though not parametrically so, for all $T \gg 4t^2/U$, as seen in the data.

Although we only analytically show the scaling of Eq. (10) to leading order in J/T and T/U (i.e., deep in the $J \ll T \ll U$ regime), numerics seems to indicate the collapse holds beyond this. Explaining this is an open problem. Despite lacking a simple analytic formula, the second-order NLCE reproduces all of the behavior, offering a simple predictive theory for the thermodynamics in the $T \gtrsim J$ regime.

The observables \mathcal{D} and \mathcal{K} show a similar universal N dependence, satisfying analogs of Eq. (10), as demonstrated in Figs. 9(a) and 9(b) by showing the collapse of \tilde{D} and \tilde{K} defined analogously to \tilde{E} . These are also reproduced by the second-order NLCE and its analytic simplifications in the temperature window of interest. The $U/t = 4$ results for \tilde{D} exhibit a window around $T = t$ where the second-order NLCE weakly breaks the collapse ($< 4\%$), but is then recovered at lower temperatures around $T/t = 0.2$, where the DQMC data collapse too. Why the $U/t = 4$ results collapse even

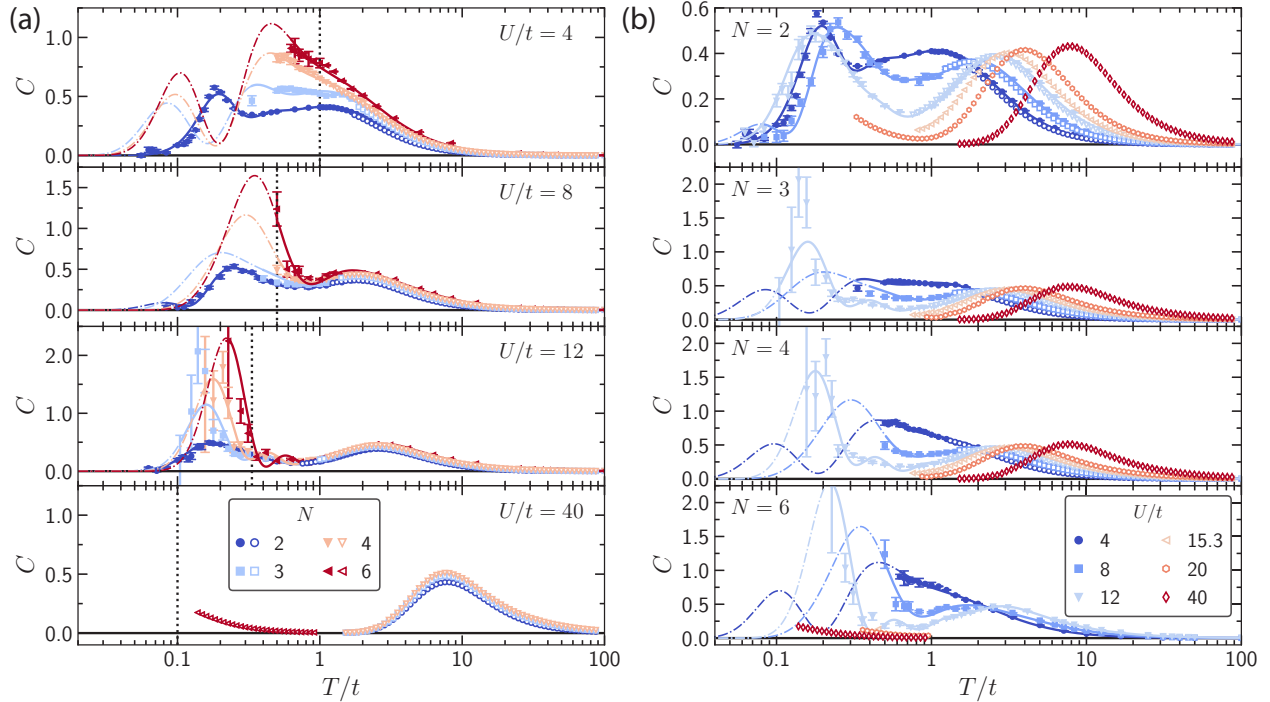


FIG. 10. Specific heat vs temperature. (a) Each panel compares C for $N = 2, 3, 4, 6$ for a fixed U/t . (b) Each panel compares C for $U/t = 4, 8, 12, 15.3, 20, 40$ for a fixed N . Solid markers are DQMC, open markers are NLCE, dotted lines correspond to the noninteracting limit, dashed lines are the zeroth-order HTSE, and solid lines come from the fits of Eq. (5) to the DQMC data in Fig. 6 down to the lowest T_n point. Thinner dash-dotted lines come from the fit in the extrapolated regime $T < \min(T_n)$, where $\{T_n\}$ is the data set of temperatures where DQMC results are obtained. Dotted vertical lines indicate the superexchange energy J .

for $T \lesssim 4t^2/U$ remains an open question and merits further exploration.

F. Temperature derivatives at unit density: $C = dE/dT$, $Ud\mathcal{D}/dT$, and dK/dT

We now present the derivatives of the energy E , interaction energy $P = U\mathcal{D}$, and the kinetic energy K . The specific heat (dE/dT) as a function of temperature is a valuable thermodynamic observable since its peaks indicate temperatures below which the entropy is significantly reduced as degrees of freedom reorganize and cease to fluctuate.

The specific heat as a function of temperature [see Fig. 10(a)] presents a two-peak structure for $N = 2$; for other N a high-temperature peak is present in all cases, and in most an upturn occurs at lower temperatures, necessitating a second peak at lower temperatures beyond the range of our calculations since $C \rightarrow 0$ as $T \rightarrow 0$. At least at large U/t , the origin of the high-temperature peak is associated with freezing of the charge fluctuations as the temperature is lowered, while the low-temperature peak is associated with the onset of spin correlations, as has been shown for $N = 2$ [100,110] and will be evident from our results on dP/dT and dK/dT . For strong interactions, the high-temperature peak is closely in agreement with the results of the zeroth-order HTSE and is roughly independent of N , with just small changes of amplitude at small U/t . The upturn of C as T/t is lowered towards a presumable low-temperature peak (though not directly accessible in the data for $N \geq 3$) depends on N and U/t . The upturn seems to grow with N , and it generally

decreases with U/t , although at the lowest temperatures, there may be a complicated nonmonotonic dependence. The extent to which the trends of the upturn are either a reflection of the temperature at which the low- T peak occurs or result from changes in the amplitude of the low- T peak cannot be assessed with the current data and is an interesting question for future theory and experiment.

The final feature of the specific heat that we analyze is motivated by the finding in Ref. [100] that the specific heat versus temperature curves cross around $T/t \approx 1.6$ for all $U/t \in [1, 10]$ for $N = 2$. Figure 10(b) shows that this remains true for other values of N , with nearly the same value of the crossing temperature. However, we note that this crossing only occurs for $U/t \lesssim 10$, and fails for $U = 15.3t$ and larger. The physical significance of this crossing is unclear. Several references [100,113–117] have seen this crossing in two dimensions (in square, honeycomb, and asymmetric [$t_\uparrow \neq t_\downarrow$] Hubbard models) at $(C^*, T^*) \approx (0.34, 1.6t)$ but all are at relatively small U/t . For small U/t Ref. [114] shows that the presence of such high- T crossing arises if one approximates two parameters as small: $1/d$ (where d is the dimension) and the integral over the deviation of the density of states from a constant value [112].

Examining the contributions dP/dT and dK/dT to the specific heat helps disentangle the contributions to the specific heat of the charge and spin degrees of freedom. In Fig. 11(a) the dP/dT data for $U/t \geq 8$ exhibit a high- T charge peak and a negative dip at lower T/t for all N . For such interactions, the high- T peak in the specific heat comes from dP/dT . For $U/t = 4$ and $N = 2$ there is a low- T peak in dP/dT ,

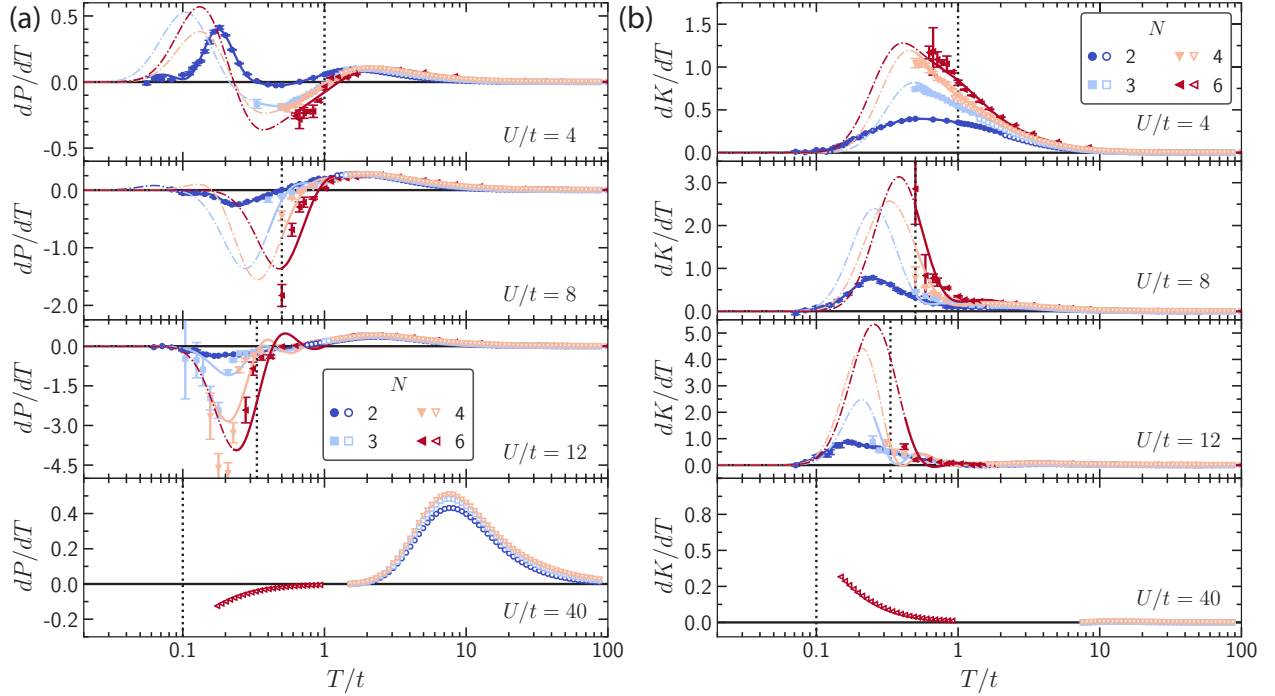


FIG. 11. Contributions to the specific heat vs temperature. Each panel compares (a) dP/dT and (b) dK/dT for $N = 2, 3, 4, 6$ for a fixed U/t . Solid markers are DQMC, open markers are NLCE, and solid lines come from the fits of Eq. (5) to the DQMC data in Figs. 3(a) and 5 down to the lowest T_n point. Thinner dash-dotted lines come from the fit in the extrapolated regime $T < \min\{T_n\}$, where $\{T_n\}$ is the data set of temperatures where DQMC results are obtained. Dotted vertical lines indicate the superexchange energy J .

which gives rise to the low- T peak in the specific heat. For $U/t = 4$ and $N > 2$, the fits suggest the existence of a dip and then a peak as temperature is lowered; however, drawing firm conclusions here requires further studies.

In Fig. 11(b) the dK/dT data for all values of the interaction strength are positive and exhibit a low- T peak or a low- T upturn which implies the existence of a peak since $dK/dT \rightarrow 0$ as $T \rightarrow 0$. The magnitude of the upturn or peak increases with N . For $U/t \geq 8$ the low- T peak (or upturn) in the specific heat arises from the spin degree of freedom, seen in dK/dT [Fig. 11(b)]. Together dP/dT and dK/dT give Fig. 10(a). These results complement the ones presented in Refs. [100,110], which demonstrate that for $N = 2$, at small U/t the low- T peak arises from dP/dT as opposed to dK/dT in the large U/t limit. The results presented here imply the same conclusion for all N studied in this work: at large U/t the low- T peak arises from dK/dT and the high- T peak from dP/dT , while at small U/t the low- T peak comes from dP/dT and the high- T peak from dK/dT .

G. Entropy at unit density: Dependence on U/t , T/t , and N

Figure 12(a) shows the N dependence of the entropy per site as a function of T for each U/t studied. For all values of the interaction strength we observe that for temperatures above the superexchange energy, at fixed entropy, the system with larger N is at a lower temperature. These results are in agreement with [104,118], highlighting that gases adiabatically loaded into an optical lattice in this regime will have a significantly lower temperature as N is increased. For

$U/t = 4$ this cooling seems to occur for all values of T/t and N . However, for $U/t \geq 8$, the curves roughly collapse below $T \lesssim 4t^2/U$, at least for $N > 2$, suggesting that for 2D square lattices, the dramatic benefits in cooling to the superexchange energy scale will be less effective when cooling well below this scale. We note that this doesn't rule out the cooling with increasing N persisting to arbitrarily low temperatures in other geometries, for example, as has been shown in 1D chains [50].

Figure 12(b) shows the same entropy per site's U dependence as a function of T for each N studied. For each N there is a crossing at finite temperature for all U/t . The location of this crossing occurs at higher entropy and T for larger N . The existence of a crossing in the entropy curves for different U/t for $N = 2$ follows from the presence of a crossing in the specific heat [100,113–117], given that $C(T, U) = T[\partial S(T, U)/\partial T]$. Our results demonstrate that such behavior is still present for $N > 2$.

IV. CONCLUSIONS

We have explored the evolution of thermodynamic observables of the SU(N) Fermi-Hubbard model as a function of temperature T , interaction strength U/t , and the number of flavors N at $\langle n \rangle = 1$. DQMC and NLCE provide accurate results over a wide range of temperatures, including temperatures roughly an order of magnitude below the tunneling t , with the exact value depending on N and U/t . Neither method is able to access arbitrarily low temperatures, but the obtained results are far beyond what is accessible to low-order HTSE methods or ED, which have serious inaccuracies even

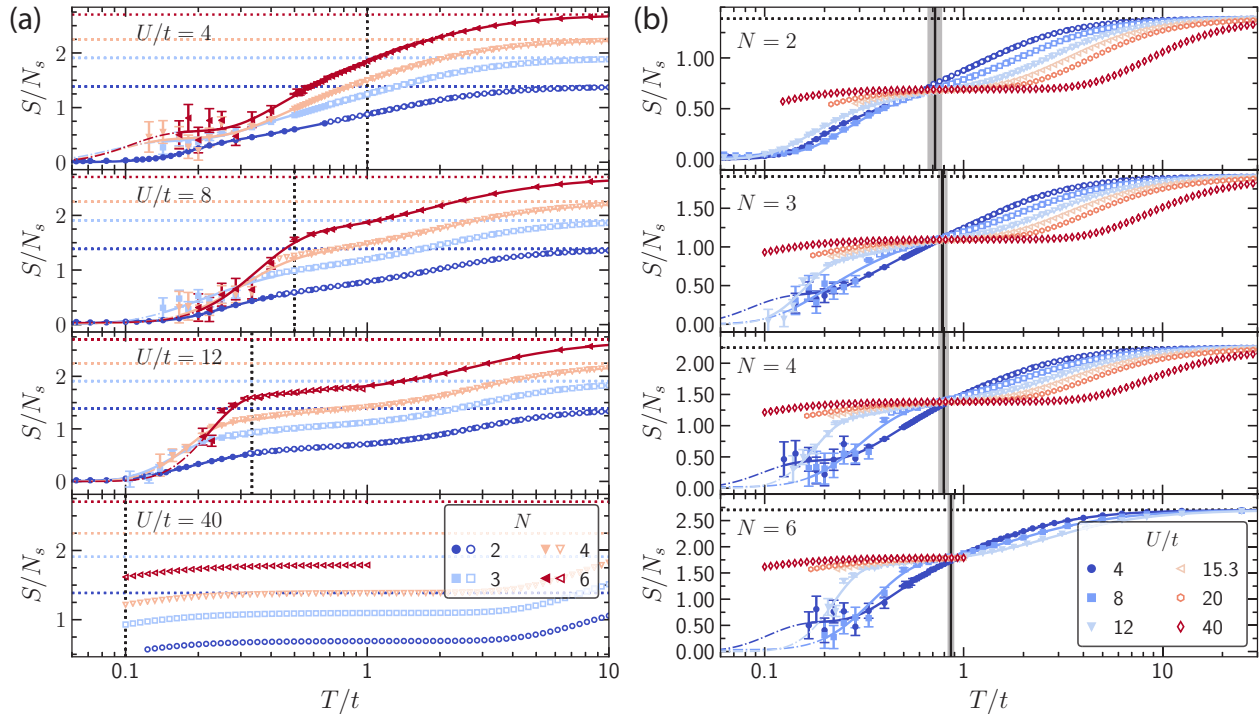


FIG. 12. Entropy per site vs temperature. (a) Each panel compares S/N_s for $N = 2, 3, 4, 6$ for a fixed U/t . (b) Each panel compares S/N_s for $U/t = 4, 8, 12, 15.3, 20, 40$ for a fixed N . Solid markers are DQMC, open markers are NLCE, and solid lines come from the fits of Eq. (5) to the DQMC data in Fig. 6 down to the lowest T_n point. Thinner dash-dotted lines come from the fit in the extrapolated regime $T < \min\{T_n\}$, where $\{T_n\}$ is the data set of temperatures where DQMC results are obtained. Dotted vertical lines indicate the superexchange energy J and solid vertical lines indicate the temperature where the different U/t curves intersect.

at $T \gtrsim 5t$. The DQMC and NLCE agree where their regimes of convergence overlap, further boosting confidence in the accuracy of the numerics. Some results were also presented in Fig. 1 for the dependence of $\langle n \rangle$, \mathcal{D} , and average determinantal sign as a function of μ/t , as well as quantities derived from these.

A striking finding is the existence of a simple scaling law with N for $T \gtrsim J$ for E , \mathcal{D} , and K . We show that this observed scaling can be reproduced by the second-order NLCE, which takes as input only one- and two-site correlations and information about the lattice geometry, and in the appropriate regime this provides analytic expressions for the observed results. Furthermore, we show that this regime is well beyond the second-order HTSE. Although the numerics cannot provide accurate results to arbitrarily low temperature, accurate results for E , K , and \mathcal{D} are attained for all N studied to temperatures where strong correlations are present. For example, the temperatures reached for all N are slightly lower than recent experiments on the 2D SU(2) FHM [76] that observed correlations that spanned the entire (~ 15 -site wide) system. Short-ranged correlations in the SU(6) FHM have been observed in Ref. [70], and longer-ranged correlations will be an interesting subject for future work. For example, Ref. [119] found a unifying pattern for all N in the Heisenberg limit at high temperatures: spin correlations are organized in shells of equal Manhattan distance and for $N = 3$, they evolve from a two sublattice structure to a three-sublattice structure as temperature is lowered. The thermodynamic results provided here provide a foundation for studying such phenomena.

Furthermore, the exploration of the specific heat and its contributions provided additional information about the N dependence of the degrees of freedom that fluctuate in the temperature regime studied, and the specialness of the $N = 2$ case, possibly due to the perfect nesting. Our results show that the behavior of C , $Ud\mathcal{D}/dT$, and dK/dT are all qualitatively similar for all N , with only the location and height of peaks shifting. The high-temperature peaks (at $T \propto U$) are roughly independent of N , while the low-temperature behavior shows a dependence on N . The details of the latter are difficult to resolve with current numerical capabilities and point to interesting future numerical and experimental directions.

Finally, the results for the entropy have important implication for the observed dramatic cooling of SU(N) FHM systems as N is increased at fixed entropy [50,67,104,118], which has been designated Pomeranchuk cooling. This has been important for achieving the lowest temperatures in Fermi-Hubbard models by using SU(6) gases [70]. Although this effect was shown theoretically at $T \gtrsim t$ using a HTSE [104] and experimentally [67,70] and theoretically in 1D down to much lower temperatures [50], our results here indicate that as one reaches very low temperatures, the cooling as N increases becomes less pronounced in 2D square lattices. In particular, Fig. 12(a) suggests that when in the regime with T well below the superexchange energy $4t^2/U$, the temperature may be nearly independent of N at fixed entropy. However, this conclusion is reached in a regime where the noise in the numerical results is large and systematic effects may not be fully under control, so further work will be important to

settle this question. Moreover, this is a lattice- and parameter-dependent phenomenon, as it is known in 1D chains that the cooling with increasing N persists to arbitrarily low temperatures [50].

ACKNOWLEDGMENTS

The work of E.I.G.P., S.D., H.W., and K.R.A.H. was supported by the NSF PHY-1848304 and the Robert A. Welch Foundation C-1872. This work was supported in part by the Big-Data Private-Cloud Research Cyberinfrastructure MRI award funded by NSF under Grant No. CNS-1338099 and by Rice University's Center for Research Computing (CRC). The work of R.T.S. was supported by Grant No. DE-SC0014671 funded by the U.S. Department of Energy, Office of Science. The work of S.T. and Y.T. was supported by a Grant-in-Aid for Scientific Research of JSPS (No. JP18H05228) and JST CREST (No. JP-MJCR1673).

APPENDIX A: CHEMICAL POTENTIAL AND ENTROPY AT FIXED DENSITY WHEN $T \rightarrow \infty$

In order to compute the entropy using the results from DQMC at fixed density $\langle n \rangle$ using Eq. (4), we need to know *a priori* what is the entropy when $T \rightarrow \infty$. This depends on the chemical potential at $T \rightarrow \infty$, which we can analytically determine from the condition that $\langle n \rangle$ is fixed. As $T/t \rightarrow \infty$, the zeroth-order HTSE captures the behavior of $\langle n \rangle$ and it can be used with the condition $\langle n \rangle = \rho$ to determine the chemical potential. When $T \gg U$, the density is $\rho = \frac{1}{Z} \sum_n n \binom{N}{n} e^{\beta \mu n}$, defining $Z = \sum_n \binom{N}{n} e^{\beta \mu n}$. Then

$$\rho = \frac{d \ln Z}{d(\beta \mu)} \quad (\text{A1})$$

$$= \frac{d}{d(\beta \mu)} \{ \ln[(1 + e^{\beta \mu})^N] \} \quad (\text{A2})$$

$$= N \frac{e^{\beta \mu}}{1 + e^{\beta \mu}}. \quad (\text{A3})$$

Solving for $\beta \mu$, we obtain

$$\beta \mu(N, \rho) = \ln \left(\frac{\rho}{N - \rho} \right). \quad (\text{A4})$$

Using this result in the zeroth-order HTSE for S gives the $T \rightarrow \infty$ entropy per site $S_\infty(N, \rho)$:

$$S_\infty(N, \rho) = \ln \left[\sum_{n=0}^N \binom{N}{n} \left(\frac{\rho}{N - \rho} \right)^n \right] - \rho \ln \left(\frac{\rho}{N - \rho} \right), \quad (\text{A5})$$

$$= N \ln \left(\frac{N}{N - \rho} \right) - \rho \ln \left(\frac{\rho}{N - \rho} \right). \quad (\text{A6})$$

APPENDIX B: CONVERGENCE OF NLCE AS NUMBER OF SITES INCREASES AND COMPARISON WITH ED

We investigate the convergence of the NLCE with expansion order, and we demonstrate that it is significantly more accurate than ED, even when the ED is performed on larger clusters (and therefore requires more computational

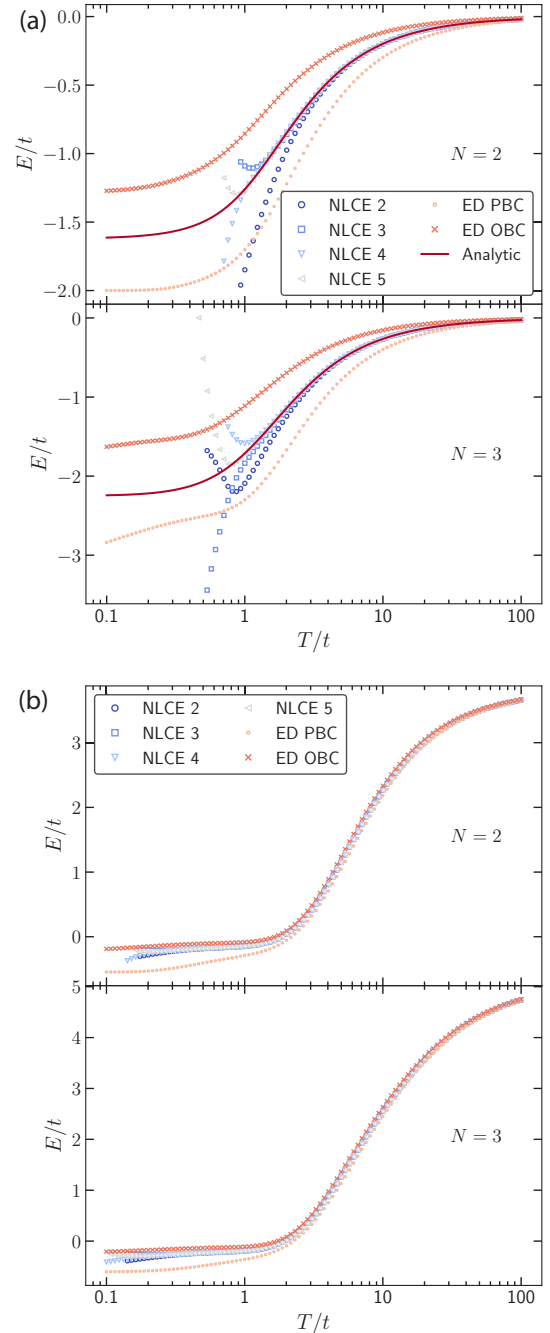


FIG. 13. Convergence of NLCE with expansion order five and comparison with ED. Energy vs T/t at $\langle n \rangle = 1$ for (a) $U = 0$ (b) $U = 15.3t$ for SU(2) and SU(3). The ED is evaluated in a 3×2 lattice for both open and periodic boundary conditions. (a) The NLCE converges to the analytic result (the solid line) to much lower T/t than either of the ED results. (b) The NLCE curves converge to each other at much lower temperatures than the ED curves collapse on each other or on the NLCE results, signaling that the NLCE converges to significantly lower temperatures than the ED.

resources) than the NLCE. We focus on two cases: $U/t = 0$ which offers an analytic solution for comparison [Fig. 13(a)] and $U/t = 15.3$ [Fig. 13(b)], both for $\langle n \rangle = 1$. Figure 13(a) shows that the six-site (3×2) ED calculations for $U = 0$, whether with open-boundary or periodic boundary conditions,

has noticeable deviations from the exact analytic result at temperatures $T/t \lesssim 20$. Even the very low-order two-site NLCE converges accurately to much lower temperature, $T/t \lesssim 3$. Increasing the order of the NLCE calculation leads to results that converge down to still lower temperature. Note that the NLCE calculation is self-diagnosing: even without appealing to the analytic result, the NLCE demonstrates its accuracy when adjacent NLCE orders agree with each other. For example, when the order four and order five results closely agree with each other, then they also agree with the analytic result. This is consistent with earlier findings in other models [90,120]. It is worth mentioning that ED results may still provide valuable information: at low- T the NLCE fails dramatically, and while the ED may not be quantitatively accurate, it may still reproduce qualitative features.

Now we show similar results for $U/t = 15.3$ where no analytic result is available. The self-diagnosis of the NLCE demonstrates the convergence of two-site NLCE to $T \sim 0.4t$, and lower temperatures upon increasing the order. Again, the NLCE converges down to a much lower temperature than the ED, which shows significant deviations due to finite-size effects already at $T/t \gtrsim 2$. These results show that even numerically inexpensive NLCE calculations (two or three sites) accurately converge to much lower temperatures than the much more expensive six-site ED.

APPENDIX C: BASIS TRUNCATION IN THE NLCE

The Hilbert space dimension for the $SU(N)$ system imposes a severe limit on ED and NLCE if implemented naively, and this difficulty increases dramatically with N : the Hilbert space dimension is 2^{NN_s} , where N_s is the number of lattice sites, reaching a nearly intractable dimension of 2^{24} already for $SU(6)$ at four sites. Accounting for the $SU(N)$ symmetries ameliorates this considerably, but the basic difficulty remains.

To alleviate these problems for $N = 6$ where the difficulties are worst, we employ a basis truncation scheme for the ED used in the NLCE; this truncation was first introduced for ED in Ref. [70], and it can provide accurate results with negligible truncation error in the physical regime we consider, $\langle n \rangle \lesssim 1$, $U/t \gtrsim 1$, and T/U not too large. To understand this scheme, note that eigenstates with significant weight on flavor-number basis states with large interaction energy will be highly suppressed in the thermal average by the Boltzmann factor for that eigenstate. Thus we restrict the basis states to those with interaction energy less than or equal to pU for a constant p that we choose to obtain sufficient accuracy while remaining computationally feasible. In addition, by a similar logic, we restrict the maximum number of particles in the cluster. In the main text, we choose $p = 3$ and a maximum particle number of six (one more particle than the maximum number of sites used in the NLCE), and the truncation error is negligible at low- T but increases as T increases (see details below).

Figure 14 illustrates the accuracy of NLCE with maximum particle number restriction, and also the new numerical issues the truncation introduces, by comparing results for maximum number of particles equal to six, eight, and 10 and the unrestricted result for $SU(3)$ at $U/t = 15.3$ and $\langle n \rangle = 1$. Results are plotted to temperatures a bit past where the truncations

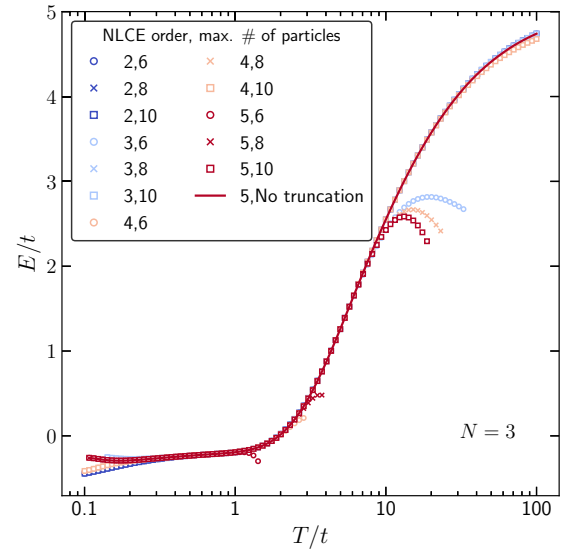


FIG. 14. Convergence of NLCE with restriction of maximum number of particles. Energy vs T/t plot at $U = 15.3t$ for $SU(3)$. Different curves are different NLCE orders from two to five, and restriction of maximum number of particles to six, eight, and ten, as indicated in the legend. The divergence of NLCE at low temperature is due to the finite order of the expansion, while the divergence at high temperature is due to particle number truncation.

are accurate so that the effects of this restriction are visible. The feature apparent from the truncation is that as the temperature is increased, the results with particle number restriction deviate from the correct answer. This is expected: as the temperature is increased, the Boltzmann weight on basis states with more particles increases. A less obvious feature is that the temperature above which the restriction fails to be accurate actually decreases as the NLCE order increases. This is because the NLCE relies on cancellation of finite-size errors when combining results from many clusters to obtain accurate results, and the number of clusters used increases with NLCE order, and thus so does the required level of cancellation. The truncation of maximum number of particles interferes with the exact cancellation and is magnified by the NLCE procedure by an amount that grows with the number of contributing clusters. Thus, there is a finite window over which the NLCE results are highly converged: the particle number truncation constrains the results to being accurate below some temperature, while the finite-size clusters used in the NLCE constraint the results to being accurate above some temperature. For the $SU(3)$ results (Fig. 14) this window is roughly from $T/t = 0.2$ to 1 for maximum number of particles of six- and five-site NLCE, as seen through comparison to the results without the restriction. We also observe that the NLCE self-diagnoses its failure due to this restriction similar to how it diagnosed the failure due to the finite number of clusters used: when results with different particle number truncations agree, the calculation is accurately converged.

Figure 15 illustrates the effects of the interaction-energy-based basis truncation on top of maximum particle number restriction to six by comparing the results for $p = 3$ and $p = 4$ truncations to the nontruncated result for $SU(3)$ at

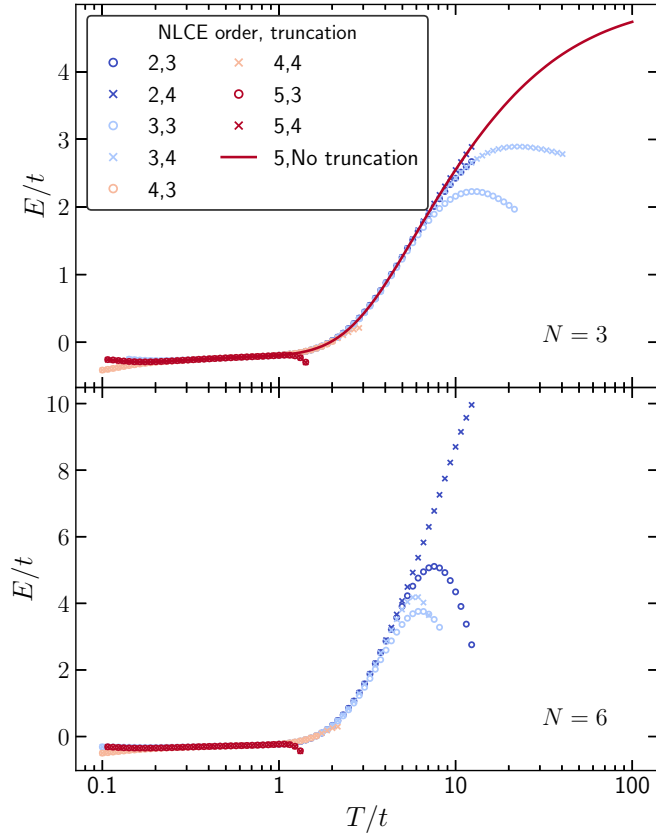


FIG. 15. Convergence of NLCE with Hilbert space truncation. Energy vs T/t plot at $U = 15.3t$ for $SU(3)$ [top] and $SU(6)$ [bottom]. The total number of particles in the cluster was restricted to six or less and basis states with interaction energy UD greater than pU were discarded. Different curves are different NLCE orders from two to five, and truncations $p = 3$ and 4 , as indicated in the legend. The divergence of NLCE at low temperature is due to the finite order of the expansion, while the divergence at high temperature is due to the basis truncation.

$U/t = 15.3$. The additional effects are negligible for NLCE orders four and five. This is not surprising since for a five-site cluster a particle number restriction of six already discards most states with highly occupied sites (doublons and higher) and a further restriction of basis states with interaction energy $< 3U$ serves mainly to discard triplon and higher states which have very small Boltzmann weights in the region of interest. Thus, this additional truncation significantly reduces computational time, while introducing negligible additional numerical errors. The self-diagnosis of the NLCE is apparent here as well, which we use to analyze the $N = 6$ results, where results without truncation are unavailable [Fig. 15 (bottom)]. When adjacent orders and different truncations agree, the NLCE is converged. We see the same trends for $N = 6$ as for $N = 3$, and a similar region of convergence for the five-site NLCE. The results in the main text thus use $p = 3$ and particle number restricted to six in the results for $N = 6$. Naturally, the value of U affects the region of convergence significantly. The size of the temperature region of convergence increases with U . For $U \leq 8t$, there is barely any region of convergence for these choices of the truncation parameters, and hence we

cannot get converged results for the $SU(6)$ system from the fifth-order NLCE with our truncation.

APPENDIX D: SECOND-ORDER NLCE CALCULATION FOR $J \ll T \ll U$: ENERGY CROSSING AND $1/N$ DEPENDENCE

In this section we focus on two things: explaining the existence of an energy crossing (as seen in Fig. 6) and demonstrating the $1/N$ scaling observed in the limit $J \ll T \ll U$. As mentioned in the main text, the second-order NLCE captures such behavior, but this does not admit a general analytic formula. However, analytic formulas can be obtained in the $J \ll T \ll U$ regime.

The second-order NLCE in the square lattice is $E = 4E^{(2)} - 3E^{(1)}$, where $E^{(x)}$ is the energy per site in an x -site system. First we demonstrate that for $J \ll T \ll U$ the one-site problem does not contribute to the energy, then we calculate the energy in the relevant particle sectors in the two-site problem, and finally we present results for their linear combination, i.e., the second-order NLCE.

1. One-site problem

In the one-site problem, the partition function is given by

$$Z^{(1)} = \sum_{n=0}^N \binom{N}{n} e^{-\beta \epsilon_0(n)}, \quad (D1)$$

where $\epsilon_0(n) = U \binom{N}{2} - \mu n$. The density $\rho^{(1)}$ is

$$\rho^{(1)} = \langle n \rangle = \frac{1}{Z^{(1)}} \sum_{n=0}^N n \binom{N}{n} e^{-\beta \epsilon_0(n)}, \quad (D2)$$

while the energy $E^{(1)}$ is

$$E^{(1)} = \langle H + \mu n \rangle = \frac{1}{Z^{(1)}} \sum_{n=0}^N U \binom{N}{2} \binom{N}{n} e^{-\beta \epsilon_0(n)}. \quad (D3)$$

Because $T \ll U$, we can obtain an analytical approximate expression for the chemical potential $\mu_0(T, U, N)$ that fixes the density to $\rho = 1$ by only considering the zero-, one-, and two-particle sectors. This expression is exact for $N = 2$, but is only true to leading order in T/U for $N > 2$, since it truncates eigenstates with triplons and higher occupancies. The solution for μ_0 is given by

$$\mu_0(T, U, N) = \frac{U}{2} + \frac{1}{2} T \ln \left[\frac{2}{N(N-1)} \right], \quad (D4)$$

and the energy in this limit is

$$E^{(1)} = \frac{U e^{-\beta U/2}}{2 + \sqrt{\frac{2N}{N-1}}} \approx 0. \quad (D5)$$

Therefore we have shown that in the $\beta U \gg 1$ limit the second-order NLCE in the square lattice is determined by the two-site result, $E = 4E^{(2)}$.

2. Two-site problem

The Hilbert space of the two-site problem is 4^N , and analytically diagonalizing such matrix—even if exploiting particle

number conservation for each spin component and spin permutation symmetry—is not possible. However, not all particle sectors need to be considered since $\beta U \gg 1$ and $\langle n \rangle = 1$. Under these two conditions, and to leading order in βJ , we can use the chemical potential from Eq. (D4) in the two-site calculation. This ensures that at $\langle n \rangle = 1$ only the two-site two-particle sector (TSTP) contributes, since all other sectors are $\propto e^{-\beta U}$, and therefore negligible.

In the TSTP, there are N states where two particles of the same flavor sit on sites 1 and 2. Since these are Pauli blocked from hopping, and there is no U contribution, they constitute N independent one dimensional subspaces of energy $\epsilon = 0$, giving rise to a contribution N in the partition function. Furthermore, there are $\binom{N}{2}$ choices where the flavors of the two particles are different. Since the hopping conserves flavor, these form independent four-dimensional subspaces with levels identical to the usual $N = 2$ spectrum in the one spin-up and one spin-down sector. Therefore, in the TSTP the partition function $Z^{(2)}$ and energy per site $E^{(2)}$ are given by

$$Z^{(2)} = N + \binom{N}{2} Z_2, \quad (\text{D6})$$

$$E^{(2)} = \frac{1}{2} \binom{N}{2} E_2, \quad (\text{D7})$$

$$Z_2 = \sum_{n=1}^4 \exp(-\beta \epsilon_n), \quad (\text{D8})$$

$$E_2 = \frac{1}{Z} \sum_{n=1}^4 \epsilon_n \exp(-\beta \epsilon_n), \quad (\text{D9})$$

where ϵ_n are the eigenvalues of the two-particle sector with different spin component, i.e., $\sigma \neq \tau$. These eigenvalues are $\epsilon_n = \{0, U, U/2 \pm \sqrt{16t^2 + U^2}\}$.

First, an energy crossing for different values of N as a function of T/t at a fixed U/t in the TSTP occurs when Eq. (D7) is equal to zero, i.e., $E_2 = 0$, to demand the N -independence of the energy. The temperature at which the crossing occurs is the solution to the following transcendental

equation:

$$0 = U e^{-\beta U} + \frac{U}{2} \left[1 + \sqrt{1 + \left(\frac{4t}{U}\right)^2} \right] e^{-\beta \frac{U}{2} [1 + \sqrt{1 + (\frac{4t}{U})^2}]} + \frac{U}{2} \left[1 - \sqrt{1 + \left(\frac{4t}{U}\right)^2} \right] e^{-\beta \frac{U}{2} [1 - \sqrt{1 + (\frac{4t}{U})^2}]}. \quad (\text{D10})$$

That this equation has solutions demonstrates the existence of a crossing point, and it qualitatively explains the trends of T^*/t with U/t , although it deviates quantitatively from the results in Fig. 7.

Now we demonstrate the $1/N$ scaling for $J \ll T \ll U$, where the second-order NLCE shows unconditionally that the collapse occurs in this regime. We present results for E , but analogous results can be obtained for \mathcal{D} and K . The energy in the TSTP is given by Eq. (D7),

$$E^{(2)}(T, U, N) = \frac{1}{2} \frac{\binom{N}{2} \sum_{n=1}^4 \epsilon_n \exp(-\beta \epsilon_n)}{N + \binom{N}{2} \sum_{n=1}^4 \exp(-\beta \epsilon_n)}. \quad (\text{D11})$$

Since $U \gg t$, the ϵ_n have simple expressions $\epsilon_n = \{0, U, U + J, -J\}$. Because $\beta U \gg 1$, $E^{(2)}$ is given to leading order by

$$E^{(2)}(T, U, N) \approx \frac{1}{2} \frac{\binom{N}{2} (-J e^{\beta J})}{N + \binom{N}{2} (1 + e^{\beta J})}, \\ = \frac{1}{2} \frac{-J e^{\beta J}}{\frac{N+1}{N-1} + e^{\beta J}}. \quad (\text{D12})$$

Finally, since in the $J \ll T \ll U$ limit $E = 4E^{(2)}$, the second-order NLCE to zeroth order in $\beta J \ll 1$ is

$$E(T, U, N) \approx -J + \frac{1}{N} J. \quad (\text{D13})$$

This demonstrates that the scaling (10) holds in the regime $4t^2/U \ll T \ll U$, when $t/U \ll 1$ to zeroth order in βJ .

-
- [1] A. Montorsi (ed.) *The Hubbard Model: A Reprint Volume* (World Scientific, Singapore, 1992).
- [2] H. Tasaki, The Hubbard model - an introduction and selected rigorous results, *J. Phys.: Condens. Matter* **10**, 4353 (1998).
- [3] D. P. Arovas, E. Berg, S. Kivelson, and S. Raghu, The Hubbard model, [arXiv:2103.12097v2](https://arxiv.org/abs/2103.12097v2) (2021).
- [4] A. Bohrdt, L. Homeier, C. Reinmoser, E. Demler, and F. Grusdt, Exploration of doped quantum magnets with ultracold atoms, [arXiv:2107.08043](https://arxiv.org/abs/2107.08043) v1 (2021).
- [5] M. Imada, A. Fujimori, and Y. Tokura, Metal-insulator transitions, *Rev. Mod. Phys.* **70**, 1039 (1998).
- [6] S. R. White, D. J. Scalapino, R. L. Sugar, E. Y. Loh, J. E. Gubernatis, and R. T. Scalettar, Numerical study of the two-dimensional Hubbard model, *Phys. Rev. B* **40**, 506 (1989).
- [7] T. Schäfer, N. Wentzell, F. Šimkovic, Y.-Y. He, C. Hille, M. Klett, C. J. Eckhardt, B. Arzhang, V. Harkov, F.-M.

Le Régent, A. Kirsch, Y. Wang, A. J. Kim, E. Kozik, E. A. Stepanov, A. Kauch, S. Andergassen, P. Hansmann, D. Rohe, Y. M. Vilk *et al.*, Tracking the Footprints of Spin Fluctuations: A Multimethod, Multimessenger Study of the Two-Dimensional Hubbard Model, *Phys. Rev. X* **11**, 011058 (2021).

- [8] M. Qin, C.-M. Chung, H. Shi, E. Vitali, C. Hubig, U. Schollwöck, S. R. White, and S. Zhang (Simons Collaboration on the Many-Electron Problem), Absence of Superconductivity in the Pure Two-Dimensional Hubbard Model, *Phys. Rev. X* **10**, 031016 (2020).
- [9] M. Qin, T. Schäfer, S. Andergassen, P. Corboz, and E. Gull, The Hubbard model: A computational perspective, [arXiv:2104.00064](https://arxiv.org/abs/2104.00064) [cond-mat.str-el] (2021).
- [10] Y. Q. Li, M. Ma, D. N. Shi, and F. C. Zhang, SU(4) Theory for Spin Systems with Orbital Degeneracy, *Phys. Rev. Lett.* **81**, 3527 (1998).

- [11] Y. Tokura, Orbital physics in transition-metal oxides, *Science* **288**, 462 (2000).
- [12] E. Dagotto, T. Hotta, and A. Moreo, Colossal magnetoresistant materials: The key role of phase separation, *Phys. Rep.* **344**, 1 (2001).
- [13] M. O. Goerbig, Electronic properties of graphene in a strong magnetic field, *Rev. Mod. Phys.* **83**, 1193 (2011).
- [14] X. Y. Xu, K. T. Law, and P. A. Lee, Kekulé valence bond order in an extended Hubbard model on the honeycomb lattice with possible applications to twisted bilayer graphene, *Phys. Rev. B* **98**, 121406(R) (2018).
- [15] Y. You and A. Vishwanath, Superconductivity from valley fluctuations and approximate SO(4) symmetry in a weak coupling theory of twisted bilayer graphene, *npj Quantum Mater.* **4**, 16 (2019).
- [16] W. M. H. Natori, R. Nutakki, R. G. Pereira, and E. C. Andrade, SU(4) Heisenberg model on the honeycomb lattice with exchange-frustrated perturbations: Implications for twistrionics and Mott insulators, *Phys. Rev. B* **100**, 205131 (2019).
- [17] Y. Da Liao, J. Kang, C. N. Breið, X. Y. Xu, H.-Q. Wu, B. M. Andersen, R. M. Fernandes, and Z. Y. Meng, Correlation-Induced Insulating Topological Phases at Charge Neutrality in Twisted Bilayer Graphene, *Phys. Rev. X* **11**, 011014 (2021).
- [18] Y.-D. Liao, X.-Y. Xu, Z.-Y. Meng, and J. Kang, Correlated insulating phases in the twisted bilayer graphene, *Chin. Phys. B* **30**, 017305 (2021).
- [19] D. V. Chichinadze, L. Classen, Y. Wang, and A. V. Chubukov, SU(4) symmetry in twisted bilayer graphene—An itinerant perspective, *arXiv:2108.05334 v1* (2021).
- [20] Y. Yamashita, M. Tomura, Y. Yanagi, and K. Ueda, SU(3) Dirac electrons in the 1/5-depleted square-lattice Hubbard model at 1/4 filling, *Phys. Rev. B* **88**, 195104 (2013).
- [21] I. Titvinidze, A. Privitera, S.-Y. Chang, S. Diehl, M. A. Baranov, A. Daley, and W. Hofstetter, Magnetism and domain formation in SU(3)-symmetric multi-species Fermi mixtures, *New J. Phys.* **13**, 035013 (2011).
- [22] A. Sotnikov and W. Hofstetter, Magnetic ordering of three-component ultracold fermionic mixtures in optical lattices, *Phys. Rev. A* **89**, 063601 (2014).
- [23] A. Sotnikov, Critical entropies and magnetic-phase-diagram analysis of ultracold three-component fermionic mixtures in optical lattices, *Phys. Rev. A* **92**, 023633 (2015).
- [24] M. Hafez-Torbati and W. Hofstetter, Artificial SU(3) spin-orbit coupling and exotic Mott insulators, *Phys. Rev. B* **98**, 245131 (2018).
- [25] M. Hafez-Torbati and W. Hofstetter, Competing charge and magnetic order in fermionic multicomponent systems, *Phys. Rev. B* **100**, 035133 (2019).
- [26] M. Hafez-Torbati, J.-H. Zheng, B. Irsigler, and W. Hofstetter, Interaction-driven topological phase transitions in fermionic SU(3) systems, *Phys. Rev. B* **101**, 245159 (2020).
- [27] W. Nie, D. Zhang, and W. Zhang, Ferromagnetic ground state of the SU(3) Hubbard model on the Lieb lattice, *Phys. Rev. A* **96**, 053616 (2017).
- [28] C. Honerkamp and W. Hofstetter, Ultracold Fermions and the SU(N) Hubbard Model, *Phys. Rev. Lett.* **92**, 170403 (2004).
- [29] W. Hofstetter, *Advances in Solid State Physics: Flavor Degeneracy and Effects of Disorder in Ultracold Atom Systems* (Springer, Berlin, 2005).
- [30] V. Unukovych and A. Sotnikov, SU(4)-symmetric Hubbard model at quarter filling: Insights from the dynamical mean-field approach, *arXiv:2107.11219 v1* (2021).
- [31] G. Chen, K. R. A. Hazzard, A. M. Rey, and M. Hermele, Synthetic-gauge-field stabilization of the chiral-spin-liquid phase, *Phys. Rev. A* **93**, 061601(R) (2016).
- [32] D. Wang, Y. Li, Z. Cai, Z. Zhou, Y. Wang, and C. Wu, Competing Orders in the 2D Half-Filled SU(2 N) Hubbard Model through the Pinning-Field Quantum Monte Carlo Simulations, *Phys. Rev. Lett.* **112**, 156403 (2014).
- [33] Z. Zhou, Z. Cai, C. Wu, and Y. Wang, Quantum Monte Carlo simulations of thermodynamic properties of SU(2 N) ultracold fermions in optical lattices, *Phys. Rev. B* **90**, 235139 (2014).
- [34] D. Wang, L. Wang, and C. Wu, Slater and Mott insulating states in the SU(6) Hubbard model, *Phys. Rev. B* **100**, 115155 (2019).
- [35] A. Golubeva, A. Sotnikov, A. Cichy, J. Kuneš, and W. Hofstetter, Breaking of SU(4) symmetry and interplay between strongly correlated phases in the Hubbard model, *Phys. Rev. B* **95**, 125108 (2017).
- [36] H. Xu, Y. Wang, Z. Zhou, and C. Wu, Mott insulating states of the anisotropic SU(4) Dirac fermions, *arXiv:1912.11791 v1* (2019).
- [37] Z. Zhou, C. Wu, and Y. Wang, Mott transition in the π -flux SU(4) Hubbard model on a square lattice, *Phys. Rev. B* **97**, 195122 (2018).
- [38] Z. Zhou, D. Wang, C. Wu, and Y. Wang, Finite-temperature valence-bond-solid transitions and thermodynamic properties of interacting SU(2 N) Dirac fermions, *Phys. Rev. B* **95**, 085128 (2017).
- [39] Z. Zhou, D. Wang, Z. Y. Meng, Y. Wang, and C. Wu, Mott insulating states and quantum phase transitions of correlated SU(2 N) Dirac fermions, *Phys. Rev. B* **93**, 245157 (2016).
- [40] Y. Ouyang and X. Y. Xu, Projection of infinite- u Hubbard model and algebraic sign structure, *arXiv:2108.04832 v2* (2021).
- [41] N. Read and D. M. Newns, On the solution of the Coqblin-Schrieffer Hamiltonian by the large- N expansion technique, *J. Phys. C: Solid State Phys.* **16**, 3273 (1983).
- [42] I. Affleck, Large- n Limit of SU(n) Quantum “Spin” Chains, *Phys. Rev. Lett.* **54**, 966 (1985).
- [43] N. E. Bickers, Review of techniques in the large- N expansion for dilute magnetic alloys, *Rev. Mod. Phys.* **59**, 845 (1987).
- [44] I. Affleck and J. B. Marston, Large- n limit of the Heisenberg-Hubbard model: Implications for high- T_c superconductors, *Phys. Rev. B* **37**, 3774 (1988).
- [45] A. Auerbach, *Interacting Electrons and Quantum Magnetism* (Springer-Verlag, New York, 1994).
- [46] Y. Yamashita, N. Shibata, and K. Ueda, SU(4) spin-orbit critical state in one dimension, *Phys. Rev. B* **58**, 9114 (1998).
- [47] R. Assaraf, P. Azaria, M. Caffarel, and P. Lecheminant, Metal-insulator transition in the one-dimensional SU(N) Hubbard model, *Phys. Rev. B* **60**, 2299 (1999).
- [48] K. Buchta, Ö. Legeza, E. Szirmai, and J. Sólyom, Mott transition and dimerization in the one-dimensional SU(N) Hubbard model, *Phys. Rev. B* **75**, 155108 (2007).

- [49] S. R. Manmana, K. R. A. Hazzard, G. Chen, A. E. Feiguin, and A. M. Rey, *SU(N)* magnetism in chains of ultracold alkaline-earth-metal atoms: Mott transitions and quantum correlations, *Phys. Rev. A* **84**, 043601 (2011).
- [50] L. Bonnes, K. R. A. Hazzard, S. R. Manmana, A. M. Rey, and S. Wessel, Adiabatic Loading of One-Dimensional *SU(N)* Alkaline-Earth-Atom Fermions in Optical Lattices, *Phys. Rev. Lett.* **109**, 205305 (2012).
- [51] L. Messio and F. Mila, Entropy Dependence of Correlations in One-Dimensional *SU(N)* Antiferromagnets, *Phys. Rev. Lett.* **109**, 205306 (2012).
- [52] S. Xu, J. T. Barreiro, Y. Wang, and C. Wu, Interaction Effects with Varying *N* in *SU(N)* Symmetric Fermion Lattice Systems, *Phys. Rev. Lett.* **121**, 167205 (2018).
- [53] M. Hermele, V. Gurarie, and A. M. Rey, Mott Insulators of Ultracold Fermionic Alkaline Earth Atoms: Underconstrained Magnetism and Chiral Spin Liquid, *Phys. Rev. Lett.* **103**, 135301 (2009).
- [54] T. A. Tóth, A. M. Läuchli, F. Mila, and K. Penc, Three-Sublattice Ordering of the *SU(3)* Heisenberg Model of Three-Flavor Fermions on the Square and Cubic Lattices, *Phys. Rev. Lett.* **105**, 265301 (2010).
- [55] M. Hermele and V. Gurarie, Topological liquids and valence cluster states in two-dimensional *SU(N)* magnets, *Phys. Rev. B* **84**, 174441 (2011).
- [56] P. Nataf and F. Mila, Exact Diagonalization of Heisenberg *SU(N)* Models, *Phys. Rev. Lett.* **113**, 127204 (2014).
- [57] P. Corboz, A. M. Läuchli, K. Penc, M. Troyer, and F. Mila, Simultaneous Dimerization and *SU(4)* Symmetry Breaking of 4-Color Fermions on the Square Lattice, *Phys. Rev. Lett.* **107**, 215301 (2011).
- [58] B. Bauer, P. Corboz, A. M. Läuchli, L. Messio, K. Penc, M. Troyer, and F. Mila, Three-sublattice order in the *SU(3)* Heisenberg model on the square and triangular lattice, *Phys. Rev. B* **85**, 125116 (2012).
- [59] D. Yamamoto, C. Suzuki, G. Marmorini, S. Okazaki, and N. Furukawa, Quantum and Thermal Phase Transitions of the Triangular *SU(3)* Heisenberg Model Under Magnetic Fields, *Phys. Rev. Lett.* **125**, 057204 (2020).
- [60] A. Keselman, B. Bauer, C. Xu, and C.-M. Jian, Emergent Fermi Surface in a Triangular-Lattice *SU(4)* Quantum Antiferromagnet, *Phys. Rev. Lett.* **125**, 117202 (2020).
- [61] X.-P. Yao, Y. Gao, and G. Chen, Topological chiral spin liquids and competing states in triangular lattice *SU(N)* Mott insulators, *Phys. Rev. Res.* **3**, 023138 (2021).
- [62] C. Wu, Hidden Symmetry and quantum phases in spin-3/2 cold atomic systems, *Mod. Phys. Lett. B* **20**, 1707 (2006).
- [63] M. A. Cazalilla, A. F. Ho, and M. Ueda, Ultracold gases of ytterbium: Ferromagnetism and Mott states in an *SU(6)* Fermi system, *New J. Phys.* **11**, 103033 (2009).
- [64] A. V. Gorshkov, M. Hermele, V. Gurarie, C. Xu, P. S. Julienne, J. Ye, P. Zoller, E. Demler, M. D. Lukin, and A. M. Rey, Two-orbital *SU(N)* magnetism with ultracold alkaline-earth atoms, *Nat. Phys.* **6**, 289 (2010).
- [65] M. A. Cazalilla and A. M. Rey, Ultracold Fermi gases with emergent *SU(N)* symmetry, *Rep. Prog. Phys.* **77**, 124401 (2014).
- [66] S. Stellmer, F. Schreck, and T. C. Killian, Degenerate quantum gases of strontium, *Annual Review of Cold Atoms and Molecules* (World Scientific, 2014), Chap. 1, pp. 1–80.
- [67] S. Taie, R. Yamazaki, S. Sugawa, and Y. Takahashi, An *SU(6)* Mott insulator of an atomic Fermi gas realized by large-spin Pomeranchuk cooling, *Nat. Phys.* **8**, 825 (2012).
- [68] C. Hofrichter, L. Riegger, F. Scazza, M. Höfer, D. R. Fernandes, I. Bloch, and S. Fölling, Direct Probing of the Mott Crossover in the *SU(N)* Fermi-Hubbard Model, *Phys. Rev. X* **6**, 021030 (2016).
- [69] H. Ozawa, S. Taie, Y. Takasu, and Y. Takahashi, Antiferromagnetic Spin Correlation of *SU(N)* Fermi Gas in an Optical Superlattice, *Phys. Rev. Lett.* **121**, 225303 (2018).
- [70] S. Taie, E. Ibarra-García-Padilla, N. Nishizawa, Y. Takasu, Y. Kuno, H.-T. Wei, R. T. Scalettar, K. R. A. Hazzard, and Y. Takahashi, Observation of antiferromagnetic correlations in an ultracold *SU(N)* Hubbard model, [arXiv:2010.07730](https://arxiv.org/abs/2010.07730) v1 (2020).
- [71] D. Tusi, L. Franchi, L. F. Livi, K. Baumann, D. B. Orenes, L. D. Re, R. E. Barfknecht, T. Zhou, M. Inguscio, G. Cappellini, M. Capone, J. Catani, and L. Fallani, Flavour-selective localization in interacting lattice fermions via *SU(N)* symmetry breaking, [arXiv:2104.13338](https://arxiv.org/abs/2104.13338) v1 (2021).
- [72] E. Altman, K. R. Brown, G. Carleo, L. D. Carr, E. Demler, C. Chin, B. DeMarco, S. E. Economou, M. A. Eriksson, K.-M. C. Fu, M. Greiner, K. R. Hazzard, R. G. Hulet, A. J. Kollár, B. L. Lev, M. D. Lukin, R. Ma, X. Mi, S. Misra, C. Monroe *et al.*, Quantum simulators: Architectures and opportunities, *PRX Quantum* **2**, 017003 (2021).
- [73] C. Gross and I. Bloch, Quantum simulations with ultracold atoms in optical lattices, *Science* **357**, 995 (2017).
- [74] I. Bloch, J. Dalibard, and S. Nascimbène, Quantum simulations with ultracold quantum gases, *Nat. Phys.* **8**, 267 (2012).
- [75] M. F. Parsons, A. Mazurenko, C. S. Chiu, G. Ji, D. Greif, and M. Greiner, Site-resolved measurement of the spin-correlation function in the Fermi-Hubbard model, *Science* **353**, 1253 (2016).
- [76] A. Mazurenko, C. S. Chiu, G. Ji, M. F. Parsons, M. Kanász-Nagy, R. Schmidt, F. Grusdt, E. Demler, D. Greif, and M. Greiner, A cold-atom Fermi-Hubbard antiferromagnet, *Nature (London)* **545**, 462 (2017).
- [77] J. Koepsell, D. Bourgund, P. Sompet, S. Hirthe, A. Bohrdt, Y. Wang, F. Grusdt, E. Demler, G. Salomon, C. Gross, and I. Bloch, Microscopic evolution of doped Mott insulators from polaronic metal to Fermi liquid, *Science* **374**, 82 (2021).
- [78] G. Ji, M. Xu, L. H. Kendrick, C. S. Chiu, J. C. Brüggengjürgen, D. Greif, A. Bohrdt, F. Grusdt, E. Demler, M. Lebrat, and M. Greiner, Coupling a Mobile Hole to an Antiferromagnetic Spin Background: Transient Dynamics of a Magnetic Polaron, *Phys. Rev. X* **11**, 021022 (2021).
- [79] R. Yamamoto, J. Kobayashi, T. Kuno, K. Kato, and Y. Takahashi, An ytterbium quantum gas microscope with narrow-line laser cooling, *New J. Phys.* **18**, 023016 (2016).
- [80] F. Schäfer, T. Fukuhara, S. Sugawa, Y. Takasu, and Y. Takahashi, Tools for quantum simulation with ultracold atoms in optical lattices, *Nat. Rev. Phys.* **2**, 411 (2020).
- [81] D. Okuno, Y. Amano, K. Enomoto, N. Takei, and Y. Takahashi, Schemes for nondestructive quantum gas microscopy of single atoms in an optical lattice, *New J. Phys.* **22**, 013041 (2020).

- [82] The number of on-site pairs and the double occupancy are equivalent in the SU(2) Fermi-Hubbard model due to Pauli exclusion principle. However, for $N > 2$ this is not the case. The number of on-site pairs \mathcal{D} counts the pairs of particles per site and is what controls the interaction energy $U\mathcal{D}$, while the double occupancy most naturally refers to the probability of configurations with exactly two particles per site, or to summing probabilities of all configurations with two or more particles per site. Either one of these is distinct from the number of on-site pairs \mathcal{D} . Computing the number of double occupancies thus requires the calculation of density fluctuations, i.e., terms of the order $\langle n^x \rangle$ with $x \in [2, N]$, which are computationally more expensive and experimentally harder to access.
- [83] Y. Nakamura, Y. Takasu, J. Kobayashi, H. Asaka, Y. Fukushima, K. Inaba, M. Yamashita, and Y. Takahashi, Experimental determination of Bose-Hubbard energies, *Phys. Rev. A* **99**, 033609 (2019).
- [84] J. Koepsell, S. Hirthe, D. Bourgund, P. Sompet, J. Vijayan, G. Salomon, C. Gross, and I. Bloch, Robust Bilayer Charge Pumping for Spin- and Density-Resolved Quantum Gas Microscopy, *Phys. Rev. Lett.* **125**, 010403 (2020).
- [85] Q. Zhou and T.-L. Ho, Universal Thermometry for Quantum Simulation, *Phys. Rev. Lett.* **106**, 225301 (2011).
- [86] T. Hartke, B. Oreg, N. Jia, and M. Zwierlein, Doubly-Hole Correlations and Fluctuation Thermometry in a Fermi-Hubbard Gas, *Phys. Rev. Lett.* **125**, 113601 (2020).
- [87] R. Blankenbecler, D. J. Scalapino, and R. L. Sugar, Monte Carlo calculations of coupled boson-fermion systems. I, *Phys. Rev. D* **24**, 2278 (1981).
- [88] S. Sorella, S. Baroni, R. Car, and M. Parrinello, A novel technique for the simulation of interacting fermion systems, *Europhys. Lett.* **8**, 663 (1989).
- [89] M. Rigol, T. Bryant, and R. R. P. Singh, Numerical Linked-Cluster Approach to Quantum Lattice Models, *Phys. Rev. Lett.* **97**, 187202 (2006).
- [90] B. Tang, E. Khatami, and M. Rigol, A short introduction to numerical linked-cluster expansions, *Comput. Phys. Commun.* **184**, 557 (2013).
- [91] R. A. Hart, P. M. Duarte, T.-L. Yang, X. Liu, T. Paiva, E. Khatami, R. T. Scalettar, N. Trivedi, D. A. Huse, and R. G. Hulet, Observation of antiferromagnetic correlations in the Hubbard model with ultracold atoms, *Nature (London)* **519**, 211 (2015).
- [92] D. Greif, T. Uehlinger, G. Jotzu, L. Tarruell, and T. Esslinger, Short-range quantum magnetism of ultracold fermions in an optical lattice, *Science* **340**, 1307 (2013).
- [93] L. W. Cheuk, M. A. Nichols, K. R. Lawrence, M. Okan, H. Zhang, E. Khatami, N. Trivedi, T. Paiva, M. Rigol, and M. W. Zwierlein, Observation of spatial charge and spin correlations in the 2D Fermi-Hubbard model, *Science* **353**, 1260 (2016).
- [94] P. T. Brown, D. Mitra, E. Guardado-Sanchez, P. Schauß, S. S. Kondov, E. Khatami, T. Paiva, N. Trivedi, D. A. Huse, and W. S. Bakr, Spin-imbalance in a 2D Fermi-Hubbard system, *Science* **357**, 1385 (2017).
- [95] P. T. Brown, D. Mitra, E. Guardado-Sanchez, R. Nourafkan, A. Reymbaut, C.-D. Hébert, S. Bergeron, A.-M. S. Tremblay, J. Kokalj, D. A. Huse, P. Schauß, and W. S. Bakr, Bad metallic transport in a cold atom Fermi-Hubbard system, *Science* **363**, 379 (2018).
- [96] Previous work applied determinant quantum Monte Carlo for the SU(2N) Fermi-Hubbard model at half-filling, i.e. $\langle n \rangle = N/2$, using an alternative Hubbard-Stratonovich decomposition. This alternative decomposition is free of the sign problem at half-filling for SU(2N) [32,33,121,122].
- [97] A sweep updates all the auxiliary fields at every lattice site and imaginary time slice.
- [98] R. T. Scalettar, R. M. Noack, and R. R. P. Singh, Ergodicity at large couplings with the determinant Monte Carlo algorithm, *Phys. Rev. B* **44**, 10502 (1991).
- [99] We used the three-point differentiation rule
- $$f'(x) = \left[\frac{x_i - x_{i+1}}{(x_{i-1} - x_i)(x_{i-1} - x_{i+1})} \right] f(x_{i-1}) + \left[\frac{2x_i - x_{i-1} - x_{i+1}}{(x_i - x_{i-1})(x_i - x_{i+1})} \right] f(x_i) + \left[\frac{x_i - x_{i-1}}{(x_{i+1} - x_{i-1})(x_{i+1} - x_i)} \right] f(x_{i+1}),$$
- with error $O(h^2)$ where h is the maximum spacing of adjacent x_i . Statistical error bars are obtained by error propagation.
- [100] T. Paiva, R. T. Scalettar, C. Huscroft, and A. K. McMahan, Signatures of spin and charge energy scales in the local moment and specific heat of the half-filled two-dimensional Hubbard model, *Phys. Rev. B* **63**, 125116 (2001).
- [101] A. McMahan, C. Huscroft, R. Scalettar, and E. Pollock, Volume-collapse transitions in the rare earth metals, *J. Comput.-Aided Mater. Des.* **5**, 131 (1998).
- [102] An equal weight on regularization and fitting terms is enough to ensure that $S \rightarrow 0$ as $T \rightarrow 0$ with an error $\lesssim 10^{-2}$ for all N and U/t .
- [103] The idea of truncating the Hilbert space is not new; see, for example, Ref. [123], where authors limit the thermal averages to a fraction of low-lying states and use the Lanczos algorithm to reduce the computational cost of full diagonalization.
- [104] K. R. A. Hazzard, V. Gurarie, M. Hermele, and A. M. Rey, High-temperature properties of fermionic alkaline-earth-metal atoms in optical lattices, *Phys. Rev. A* **85**, 041604(R) (2012).
- [105] C. J. Pethick and H. Smith, *Bose-Einstein Condensation in Dilute Gases* (Cambridge University Press, Cambridge, 2008).
- [106] V. I. Iglovikov, E. Khatami, and R. T. Scalettar, Geometry dependence of the sign problem in quantum Monte Carlo simulations, *Phys. Rev. B* **92**, 045110 (2015).
- [107] G. G. Batrouni and R. T. Scalettar, Anomalous decouplings and the fermion sign problem, *Phys. Rev. B* **42**, 2282 (1990).
- [108] G. G. Batrouni and P. de Forcrand, Fermion sign problem: Decoupling transformation and simulation algorithm, *Phys. Rev. B* **48**, 589 (1993).
- [109] S.-S. B. Lee, J. von Delft, and A. Weichselbaum, Filling-driven Mott transition in SU(N) Hubbard models, *Phys. Rev. B* **97**, 165143 (2018).
- [110] E. Ibarra-García-Padilla, R. Mukherjee, R. G. Hulet, K. R. A. Hazzard, T. Paiva, and R. T. Scalettar, Thermodynamics and magnetism in the two-dimensional to three-dimensional crossover of the Hubbard model, *Phys. Rev. A* **102**, 033340 (2020).

[111] In the $T \rightarrow \infty$ limit, at $\langle n \rangle = 1$, the number of on-site pairs is given by

$$\mathcal{D}_\infty = \frac{1}{2} \sum_{\sigma \neq \tau} \langle n_\sigma \rangle \langle n_\tau \rangle = \binom{N}{2} \frac{1}{N^2} = \frac{1}{2} \left(1 - \frac{1}{N} \right),$$

where we used that $\langle n_\sigma \rangle = \langle n \rangle / N$ because of the $SU(N)$ symmetry.

- [112] M. Greger, M. Kollar, and D. Vollhardt, Isosbestic points: How a narrow crossing region of curves determines their leading parameter dependence, *Phys. Rev. B* **87**, 195140 (2013).
- [113] D. Vollhardt, Characteristic Crossing Points in Specific Heat Curves of Correlated Systems, *Phys. Rev. Lett.* **78**, 1307 (1997).
- [114] N. Chandra, M. Kollar, and D. Vollhardt, Nearly universal crossing point of the specific heat curves of Hubbard models, *Phys. Rev. B* **59**, 10541 (1999).
- [115] D. Duffy and A. Moreo, Specific heat of the two-dimensional Hubbard model, *Phys. Rev. B* **55**, 12918 (1997).
- [116] C. A. Macedo and A. M. C. de Souza, Crossing points in specific-heat curves of the asymmetric Hubbard model, *Phys. Rev. B* **65**, 153109 (2002).
- [117] T. Paiva, R. T. Scalettar, W. Zheng, R. R. P. Singh, and J. Oitmaa, Ground-state and finite-temperature signatures of quantum phase transitions in the half-filled Hubbard model on a honeycomb lattice, *Phys. Rev. B* **72**, 085123 (2005).
- [118] A. M. Müller, M. Lajkó, F. Schreck, F. Mila, and J. Minář, State selective cooling of $SU(N)$ Fermi gases, *Phys. Rev. A* **104**, 013304 (2021).
- [119] C. Romen and A. M. Läuchli, Structure of spin correlations in high-temperature $SU(N)$ quantum magnets, *Phys. Rev. Res.* **2**, 043009 (2020).
- [120] E. Khatami and M. Rigol, Thermodynamics of strongly interacting fermions in two-dimensional optical lattices, *Phys. Rev. A* **84**, 053611 (2011).
- [121] F. F. Assaad, $SU(2)$ -spin invariant auxiliary field quantum Monte Carlo algorithm for Hubbard models, [arXiv:cond-mat/9806307](https://arxiv.org/abs/cond-mat/9806307) v1 (1998).
- [122] F. F. Assaad, Phase diagram of the half-filled two-dimensional $SU(N)$ Hubbard-Heisenberg model: A quantum Monte Carlo study, *Phys. Rev. B* **71**, 075103 (2005).
- [123] K. Bhattaram and E. Khatami, Lanczos-boosted numerical linked-cluster expansion for quantum lattice models, *Phys. Rev. E* **100**, 013305 (2019).